# Semi-coupled resolved CFD–DEM simulation of powder-based selective laser melting for additive manufacturing

Tao Yu, Jidong Zhao*

*Hong Kong University of Science and Technology, Clearwater Bay, Kowloon, Hong Kong*

## Abstract

We present a semi-coupled resolved Computational Fluid Dynamics (CFD) and Discrete Element Method (DEM) to simulate a class of granular media problems that involve thermal-induced phase changes and particle–fluid interactions. We employ an immersed boundary (IB) method to model the viscous fluids surrounding solid particles in conjunction with a fictious CFD domain occupied by the actual positions of the particle. Heat transfers between the actual fluids and the fictitious particle are treated as a multiphase problem by the CFD to resolve the temperature gradient distribution within each granular particle and its possible phase change (e.g., melting or partial melting). The mechanical interactions between the solid particles and the fluids are modeled by coupled DEM and CFD. The proposed method is validated by simulations of a typical powder-based selective laser melting (PB-SLM) process. Three key SLM input parameters, laser power, laser energy distribution and hatch distance, are examined on the effect of melting. The simulation results capture key features and observations of PB-SLM found in experiments and are quantitatively consistent with available testing data. The study provides a physically based, high-fidelity computational approach for future PB-SLM additive manufacturing.
© 2021 Elsevier B.V. All rights reserved.

*Keywords:* Granular media; Coupled CFD–DEM; Immersed Boundary Method; Multiphase modeling; Selective laser melting; Additive manufacturing

## 1. Introduction

Additive manufacturing (AM), also widely known as 3D printing (3DP), has been widely considered as a technology paving the way for the next industrial revolution towards the ultimate '*direct digital manufacturing*' (DDM) [1]. It helps to eliminate various constraints in conventional manufacturing industries that hinder optimal design, creativity and ease of manufacturing [2,3]. Among many, selective laser melting (SLM) represents a typical powder-based additive manufacturing technology using high-power lasers to melt metallic powders layer by layer to form a desired product. It features short manufacturing circle, low costs, better molding accuracy and mechanical properties [4], and has seen great potentials for application in a wide range of engineering and industries, such as the printing of aerospace components [5,6], biomedical implants [7,8]. and polymers [9]. Its future developments and wide applications, however, hinge crucially upon overcoming a number of technical barriers, including the

---

* Corresponding author.
  *E-mail address:* jzhao@ust.hk (J. Zhao).

**Table 1**

Typical experimental studies of powder based SLM.

| Variables | Typical specific factors | |
|---|---|---|
| Powder layer | Grain size distribution [27,28] | Powder layer thickness [29,30] |
| | Radius ratio of laser and powder [28] | Preheating temperature [31] |
| Laser beam | Laser energy density [28,32,33] | Energy distribution [34] |
| | Hatch distance [18,35] | Scanning strategy [36–39] |
| Material type | Printing materials (Aluminum, stainless steel, Ti-6Al-4V, inconel) [40,41] | |

poor surface roughness control caused by the balling effect, the spatter and "stair step" effect [10], and locally poor mechanical properties of built parts [11] caused by pores [12], cracking, residual stresses, and distortion [13]. Both experimental and numerical studies have been attempted to address these outstanding challenges in advancing the SLM technology to new levels [14–17].

The experimental studies have been focused on probing the printing effects of various controlling parameters pertaining to the powder layer, laser beam and material type, such as laser scanning speed, layer thickness and energy density [18,19], as summarized in Table 1. These tests indicate that low laser energy density may cause undesirable high porosity, cracking and surface defects [20,21], while optimal energy density can help ensure high quality melting of powders and formation of underlying base-plate bonding [22]. Excessive use of energy density, however, may possibly amplify the material evaporation and spattering [23] and result in the formation of pores in the built parts [24]. These experimental studies have helped to provide key insights into the understanding and optimization of practical printing procedures for quality control of the built parts. Nevertheless, experimental investigations of SLM commonly follows a trial and error approach which renders them costly, inefficient and less rigorous [25]. Numerical simulations have become a popular alternative in providing cost-effective, repeatable, systematic investigations of the entire manufacturing process for defect detection and facilitate seamless integrations with practical construction and optimization of printing model [26].

Numerical modeling of SLM has proved to be challenging due to the complicated multi-phase, multi-physics nature manifested in the thermal-induced phase transformation processes. Table 2 offers a condensed summary of major computational approaches proposed for SLM simulations and their limitations. Among these methods, the Computational Fluid Dynamics (CFD) has been particularly popular and successful in reproducing a wide range of observed features during the melting process [42] pertaining to the surface roughness [43] and pores [44], including the evolution of temperature and melt pool, and thermo-mechanical effects such as recoil pressure, Marangoni's flow and Plateau–Rayleigh instability [12,45]. One straightforward approach is to consider the powder bed as a continuum media and simulate it by CFD with spatially varying effective thermomechanical properties and other features [42,46,47], such as powder conductivity [47,48], radiation [49,50] and laser absorption [29,51]. More recently, the CFD has been further coupled with the Discrete Element Method (DEM) [25,26] to model the powder bed as discrete particle packings for simulation of such processes as powder layering process [52] and interactions with ambient gas [53]. A popular class of the coupling methods is called unresolved CFD–DEM which typically assumes an average particle diameter smaller than the CFD cell size and considers the coupling via empirical drag force models [54]. Due to its inherent limitations, the unresolved CFD–DEM cannot fully resolve the flow behavior around the particles and may not accurately capture the motions of particles motion during the melting process. In addition to the above, the SLM has also been treated by such methods as SPH and OTM in conjunction with DEM [17,55–62] which are also summarized in Table 2.

In this study, we present a semi-coupled resolved CFD–DEM to solve a class of granular media problems that involve thermal-induced phase changes and particle–fluid interactions, exemplified by the powder-based melting process of SLM. We employ the Immersed boundary (IB) method [112] to model the viscous fluids surrounding each solid particle in conjunction with a fictious CFD domain occupying the actual position of particle. Heat transfers between the actual fluids and the fictitious particles are conveniently solved as a multiphase problem by the CFD only, to resolve the temperature gradient distribution within a granular particle and associated possible phase change processes (e.g., melting or partial melting). The mechanical interactions between the particles and the fluids are considered by numerical coupling of interaction forces between the DEM and CFD. Fully resolved CFD is developed with smaller CFD grid and accurate drag force model to resolve the dynamics of fluids surrounding particles. As

**Table 2**

Summary of major players on computational modeling of SLM.

| Primary institution | Method and software | Ambient gas | Laser model | Powder layering | Multiple layers | Missing crucial phenomena |
|---|---|---|---|---|---|---|
| Ohio State University (2009–2016 [63–68]) | CFD[b] *Flow-3D* | ✔ | III[a] | III | ✔ | No metal vapor and powder motion |
| University of Erlangen–Nuremberg (2010–2014 [69–73]) | CFD *OpenFOAM* | × | I | × | × | No metal vapor and powder motion |
| University of Erlangen–Nuremberg (2011–2018 [69–74,74–88]) | LBM *waLBerla* | × | III | III | ✔ | No radiation, Marangoni term, metal vapor and powder motion |
| ESI Software Germany GmbH (2012–2019 [89–97]) | CFD *ESI_ACE+* | ✔ | III | II | × | No metal vapor and powder motion |
| UC Berkeley (2013–2019 [55–61]) | DEM & Continuum method | × | I | II | × | Simplified metal vapor, and no recoil pressure and Marangoni term |
| Lawrence Livermore National Laboratory (2014–2019 [12,47,98–106]) | CFD *ALE3D* | × | I | III | × | Simplified powder motion, and no mushy zone and metal vapor |
| University of Birmingham (2015–2018 [29,107–110]) | CFD *OpenFOAM* | × | III | III | × | No powder motion |
| UC Berkeley (2018 [17]) | SPH | × | I | III | × | No metal vapor and powder motion. |
| Peking University (2018 [52]) | CFD *OpenFOAM* | ✔ | III | III | ✔ | No recoil pressure, metal vapor and powder motion |
| Nanyang Technological University (2018 [111]) | CFD *OpenFOAM* | ✔ | II | III | × | No metal vapor and powder motion |
| Leibniz University of Hannover (2019 [62]) | OTM | ✔ | I | III | × | No metal vapor and powder motion. |
| Hong Kong University of Science and Technology (Present) | CFD&DEM *OpenFOAM* *LIGGGHTS* | ✔ | II | I | ✔ | No metal vapor |

[a]Note: I, II, III represent complete, moderate, and simple, respectively.

[b]Terminologies: SPH: Smoothed Particle Hydrodynamics; OTM: Optimal Transportation Meshfree; CFD: Computational Fluid Dynamics; DEM: Discrete Element Method; LBM: Lattice Boltzmann Method.

will be demonstrated, the proposed approach is capable of considering key physical features in SLM, such as the laser penetration, recoil pressure, Marangoni's flow, and Darcy's effects, and the effects of laser power, laser energy distribution and hatch distance, as observed in experiments. It also expedites the simulation of repeated powder layering process featured by complicated interactions among the roller, the standby powders, and the previously melted layers, with full capability of integrated evaluation of the mechanical performance of final printed parts.

## 2. Methodology: A coupled CFD-DEM approach for SLM

A coupled CFD–DEM approach is employed to simulate both the layering process and the melting process in a typical powder-based selective laser melting in this study. Two physical flow processes in the SLM of powders are broadly distinguished and treated separately, namely, the granular particle flow in an ambient gas over the solidified molten layer during the powder layering process and the multiphase thermal-fluid flow and thermal-induced phase changes during the melting process. The particle flow in an ambient gas and over a solidified molten layer during the layering process is simulated using an unresolved CFD–DEM by virtue of its high computational efficiency, whereas the multiphase thermal-fluid flow and thermal-induced phase changes during the melting process are tackled by a semi-coupled resolved CFD–DEM for higher resolution and better accuracy. The combination of the two approaches enables us to simulate the entire SLM process to obtain an accurate thermal field for both the particles and fluids and to capture crucial physical processes in SLM, including the buoyancy force, Darcy's effects, surface tension, Marangoni's flow, and recoil pressure [113]. The following presents the formulations and solution procedures of the proposed methods.

## 2.1. Unresolved coupled CFD-DEM for simulation of powder layering

An unresolved coupled CFD and DEM is proposed to simulate a typical powder layering process for preparation of laser melting. As a conventional coupling approach between CFD and DEM, the unresolved coupling formulation is based on exchange of empirical estimation of interaction forces, such as the drag force [114], between the CFD and DEM solutions for the fluid and particle phases, respectively. The approach typically adopts a CFD grid size at least three times larger than the particle diameter in the DEM [52] to ensure reasonable accuracy and numerical stability. There may be multiple powder particles resting in one CFD cell, such that the flow behavior among the particles cannot be fully resolved but can only be estimated averagely over the cell.

For a typical powder layering process, the primary interest is to establish a mechanically stable layer of granular powders for preparation of the subsequent laser melting, whereas the air flow may be less important. Hence the unresolved coupled CFD–DEM is a suitable choice. Indeed, we elect to solve the layering process by the unresolved CFD–DEM specifically for a two-fold consideration. (1) It is assumed that the underlying molten track has been solidified during the layering process where the particles will only collide with the solidified metal layer rather than the molten flow, e.g., the interaction between them can be simplified as a particle–wall interaction. (2) When the laser beam is withdrawn, the temperature of the molten track may drop to the room temperature quickly, which will not further affect the particle motion and could be ignored in the unresolved CFD–DEM. Therefore, the unresolved CFD–DEM is considered sufficiently accurate to solve the motion of the powder flow while maintaining great computational efficiency. Note that the following formulation has been presented sufficiently general to allow possible future extensions, e.g., to consider powder grains interacting with a molten track remaining in a fluid state.

In this method, it is assumed the motion of each granular powder particle is governed by the following linear and angular momentum equations and will be resolved by DEM:

$$
\begin{cases}
m_p \dfrac{d\mathbf{v}_p}{dt} = \sum \mathbf{F}_{p-p} + \sum \mathbf{F}_{p-w} + m_p \mathbf{g} + \mathbf{F}_f \\[2mm]
\mathbf{I}_p \dfrac{d\omega_p}{dt} = \sum \mathbf{M}_t + \sum \mathbf{M}_r
\end{cases}
\tag{1}
$$

where $m_p$ and $I_p$ denote respectively the mass and rotational inertia of Particle $p$. $\mathbf{g}$ is the gravitational acceleration. $F_{p-p}$ and $F_{p-w}$ are the particle–particle interaction force and particle–wall interaction force [115,116], respectively. $M_t$ and $M_r$ are the torque from tangential force and rolling friction toque, respectively [117]. $\mathbf{F}_f$ is the particle–fluid interaction force [118] including both drag force $\mathbf{F}_d$ and buoyancy force $\mathbf{F}_b$ for a general case. The drag force exerted on the particle by its surrounding fluids which is considered as the dominant interaction force between powder particles and surrounding fluid. Other interaction forces, such as inertial force, may be important depending on the specific applications [119] but will be neglected in this study.

The drag force $\mathbf{F}_d$ is calculated according to the following Hill–Koch formulation [120] and the buoyancy force $\mathbf{F}_b$ is derived from the average density based expression [121]:

$$
\begin{cases}
\mathbf{F}_d = \dfrac{V_p \beta}{\varepsilon_p} \left( \mathbf{u}_f - \mathbf{v}_p \right) \\[2mm]
\mathbf{F}_b = \rho_f V_p \mathbf{g}
\end{cases}
\tag{2}
$$

where $V_p$ is the volume of the particle. $\rho_f$ and $u_f$ are the density and velocity of the fluid, respectively. $\varepsilon_p$ is the particle void fraction in one cubic cell, and $\beta$ denotes an empirical coefficient related to $\varepsilon_p$ and the Reynolds number [122].

In the unresolved coupled CFD–DEM, the CFD will solve the following locally average Navier–Stokes equation over each fluid cell [118]:

$$
\begin{cases}
\dfrac{\partial}{\partial t} \left( \varepsilon_p \rho_f \right) + \nabla \cdot \left( \varepsilon_p \rho_f \mathbf{u}_f \right) = 0 \\[2mm]
\dfrac{\partial}{\partial t} \left( \varepsilon_p \rho_f \mathbf{u}_f \right) + \nabla \cdot \left( \varepsilon_p \rho_f \mathbf{u}_f \mathbf{u}_f \right) - \varepsilon_p \nabla \left( \mu \nabla \mathbf{u}_f \right) = -\nabla p - \mathbf{f}_p + \varepsilon_p \rho_f \mathbf{g}
\end{cases}
\tag{3}
$$

where $\mu$ is the fluid viscosity and $p$ is the fluid pressure. $\mathbf{f}_p$ is the interaction force the particles inside the cell exert on the fluid, which can be written as:

$$
\mathbf{f}_p = \sum_{i=1}^{n_j^p} D(\mathbf{r}_i - \mathbf{r}_j) \frac{(\mathbf{F}_d + \mathbf{F}_b)_i}{V_j}
\tag{4}
$$

where $n_j^{\mathrm{p}}$ is the total number of particles in cell $j$. $D(\mathbf{r}_i - \mathbf{r}_j)$ is a distribution function [122] of the position vector of the particles $\mathbf{r}_i$ and the cell center $\mathbf{r}_j$. $V_j$ is the cell volume of cell $j$.

The unresolved coupled CFD–DEM follows the following general solution procedure [118]:

(1) Set the initial and boundary conditions for the CFD and the DEM solvers.
(2) Evaluate the velocity field $\mathbf{u}_{\mathrm{p}}$ of the fluid and pressure field $p$ solving the Navier–Stokes equation without the source term $\mathbf{f}_{\mathrm{p}}$, neglecting the physical existence of particles.
(3) Calculate the drag force exerted to a particle according to the evaluated $\mathbf{u}_{\mathrm{f}}$ and $p$ and solve particle movements in Eq. (1) by DEM.
(4) Evaluate the source term $\mathbf{f}_p$ based on the DEM solution such as the positions and velocities of particles and solve the Navier–Stokes equation (3) to provide updated velocity and pressure field.
(5) Proceed to next time step and repeat steps (3) and (4).

## 2.2. Semi-coupled resolved CFD-DEM for the melting process

The melting of granular powder layer subjected to heating of a moving laser beam involves complicated multi-phase, multi-physics processes featured by thermal transfer and thermal-induced phase transformation, and solid–fluid–air interactions during their respective motions. Specifically, the heating of high-energy laser beam may generate high temperature gradients within the powder grains that lead to full (in mid track) or partial (sidetrack) melting of powders within the beam region. Driven by both Marangoni effect and recoil force (to be explained later), the molten grains may flow viscously in preferential directions, push the motion of surrounding powders, and form complex surface and inhomogeneous thermal fields during the gradual cooling process.

To address the aforementioned challenges in simulating the melting process, a semi-coupled resolved CFD–DEM method is proposed in this study. Specifically, the fully resolved coupled CFD–DEM based on the Immersed Boundary (IB) method will be employed to resolve the velocity and pressure fields of the molten flow and the driven motion of powder grains, whereas a dual-phase CFD is used to solve the thermal field including both fluid and solid grains for the entire domain. The IB method is developed as the CFD solver in the fully resolved CFD–DEM here to simulate the fluid flow around each solid particle. It requires a much smaller grid size that is at least smaller than one eighth of the particle diameter [123], providing an accurate prediction of the drag force based on the approach published by Shirgaonkar et al. [112] and hence more accurate flow behavior. Similar to the unresolved coupled CFD–DEM, the fully resolved approach solves the fluids and particles separately at first. It then considers the fluid–particle interactions by adding a force term derived from the presence of the solid particles that occupy their real physical space to the Navier–Stokes equations to perform a correction for the velocity field of the fluid for the solution [124]. However, a direct consideration of thermal transfer between the fluid and grain phases by CFD and DEM may incur inaccurate thermal field, due mainly to the limitation that one DEM particle can only have one single temperature, unless exceedingly complicated and costly treatments for each particle is made (e.g., by refining each particle to small elements [125]). In avoiding these technical difficulties, a multi-phase CFD approach is employed to solve the thermal field in this study. A fictious CFD domain occupied by the actual position of particles is created as one phase and the actual molten flow as another. In so doing, the heat transfers between the actual fluids and the fictitious particle domain can be resolved, with full respect of the temperature gradient within each individual solid particle. Consequently, both partial melting and full melting of powder grains can be simulated with the obtained high-resolution thermal field for all phases. For example, if in one metallic particle, the temperature of some of its CFD cells is higher than the solidus temperature, these cells of the particle will be deleted from the DEM domain and be replaced by high viscous fluids with the same initial shape in the CFD. As such, partial melting can be modeled. Consequently, the combination of the fully resolved coupled CFD–DEM and the multi-phase CFD is termed herein as the *semi-coupled resolved CFD–DEM* which enables us to exploit both the advantages of CFD and DEM to simulate the melting process appropriately.

In the semi-coupled resolved CFD–DEM, the particle–fluid interaction force exerted on each particle of the DEM solver is computed according to the following expression proposed by Shirgaonkar et al. [112],

$$\mathbf{F}_{\mathrm{f}} = \sum_{j \in T_{\mathrm{h}}} \left( -\nabla p + \mu \rho_{\mathrm{f}} \nabla^2 \mathbf{u}_{\mathrm{f}} \right)_j \cdot V_j \tag{5}$$

where $p$ is the fluid pressure, $\boldsymbol{u}_\text{f}$ is the velocity of the fluids, $V_j$ is the volume of cell $j$, and $T_\text{h}$ is the set of all particle-covered cells.

The multiphase flow has commonly been solved by the volume of fluid (VOF) method using volume fraction $\alpha_i$ to represent the co-existence of different phases in the domain. However, VOF can only obtain a smeared interphase between different phases which requires a specific, complicated scheme to capture the sharp interface. For example, the default scheme in *OpenFOAM*, MULES, employs a compressive flux term added into the advection equation to compress the interface. In this study, a relatively new scheme called iso-Advector [126] is used to obtain the complicated surface morphology of the melt flow featured with ripples, pores, denudation and balling effect in SLM. In this scheme, isosurfaces are first reconstructed for the cells containing the interface to compute accurate surface flux, the integral of which is then used to obtain the volume fraction field for next time step. A bounding procedure is further applied to limit the values of volume fraction within specified range, which leads to the final interface. Various classical validation tests [127,128] have demonstrated that the iso-Advector scheme offers more accurate predictions on the interface between two phases than the MULES scheme.

To facilitate the following presentation, we denote the volume fractions of the melt flow and the ambient gas in a fluid cell for the fluid phase as $\alpha_1$ and $\alpha_2$, respectively. Their relationship and the corresponding average density $\rho$ and equivalent viscosity $\mu$ [108] over the entire domain could be written as

$$\begin{cases} \alpha_1 + \alpha_2 = 1 \\ \rho = \alpha_1 \rho_1 + \alpha_2 \rho_2 \\ \mu = \alpha_1 \mu_1 + \alpha_2 \mu_2 \end{cases} \tag{6}$$

Notably, these two physical parameters in Eq. (6) can be only used in the momentum equation if the semi-coupled resolved CFD–DEM is employed. The presence of solid particles represented by a separate solid fraction $\varepsilon_\text{p}$ should also be considered when solving the thermal field. For certain cell under consideration, a solid fraction $\varepsilon_\text{p}$ of 0 and 1 indicates respectively that this cell is inside or outside the DEM particle. Consideration of $\varepsilon_\text{p}$ leads to the following revised expressions for the density $\rho_\text{T}$, dynamic viscosity $\mu_\text{T}$, thermal conductivity $k$, and heat capacity $C$ to be used in the temperature equation

$$\begin{cases} \rho_\text{T} = (\alpha_1 + 1 - \varepsilon_\text{p})\rho_1 + (\alpha_2 - 1 + \varepsilon_\text{p})\rho_2 \\ \mu_\text{T} = (\alpha_1 + 1 - \varepsilon_\text{p})\mu_1 + (\alpha_2 - 1 + \varepsilon_\text{p})\mu_2 \\ C = (\alpha_1 + 1 - \varepsilon_\text{p})\dfrac{\rho_1}{\rho}C_1 + (\alpha_2 - 1 + \varepsilon_\text{p})\dfrac{\rho_2}{\rho}C_2 \\ k = (\alpha_1 + 1 - \varepsilon_\text{p})k_1 + (\alpha_2 - 1 + \varepsilon_\text{p})k_2 \end{cases} \tag{7}$$

where the subscripts denote different phases.

The flow dynamics of the fluid phase during both the layering and melting processes is assumed to be governed by the Navier–Stokes equation. However, the momentum equation to be solved by the semi-coupled resolved CFD–DEM presents the following form,

$$\begin{aligned} \frac{\partial}{\partial t}(\rho_\text{f}\mathbf{u}_\text{f}) + \nabla \cdot (\rho_\text{f}\mathbf{u}_\text{f} \otimes \mathbf{u}_\text{f}) = {}& -\nabla p + \nabla \cdot (\mu \cdot (\nabla \mathbf{u}_\text{f})) \\ & - K_\text{c}\frac{(\alpha_1 - \alpha_\text{m})^2}{\alpha_\text{m}^3 + C_\text{k}}\mathbf{u}_\text{f} + c \cdot \sigma \cdot |\nabla \alpha_1| \frac{2\rho}{\rho_1 + \rho_2}\mathbf{n} \\ & + 0.54 p_0 \exp\left(L_\text{v} \cdot M \frac{T - T_\text{LV}}{RTT_\text{LV}}\right)|\nabla \alpha_1|\frac{2\rho}{\rho_1 + \rho_2}\mathbf{n} \\ & + \frac{d\sigma}{dT}(\nabla T - \mathbf{n}(\mathbf{n} \cdot \nabla T))|\nabla \alpha_1|\frac{2\rho}{\rho_1 + \rho_2} \end{aligned} \tag{8}$$

where $p$ is the fluid pressure, $K_\text{c}$ is the permeability coefficient, $C_\text{k}$ is a constant to avoid division by zero, $\alpha_\text{m}$ is the volume fraction of the molten metal which can be approximated using a Gaussian error function [52], $\alpha_\text{m} = \frac{\alpha_1}{2}\left[1 + \text{erf}\left(\frac{4}{T_1 - T_\text{s}}\left(T - \frac{T_1 + T_\text{s}}{2}\right)\right)\right]$, $T_1$ is the liquidus temperature, $T_\text{s}$ is the solidus temperature, $c$ is the curvature of the fluid–gas interface, $c = -\nabla \cdot \mathbf{n}$, $\mathbf{n}$ is the unit normal vector at the interface, $\mathbf{n} = \nabla \alpha_1 / |\nabla \alpha_1|$, $\sigma$ is the coefficient of surface tension, $L_\text{v}$ is the latent heat of vaporization, $M$ is the molar mass, $T$ is the temperature, $T_\text{LV}$ is the boiling temperature, $R$ is the universal gas constant. $|\nabla \alpha_1|$ is an interface term to transform a surface

force per unit area into a volumetric surface force [111,129,130]. $2\rho/(\rho_1+\rho_2)$ is a sharp surface force term to smear out between two phases [108,131]. $d\sigma/dT$ represents the change of surface tension coefficient with the temperature and it is considered as a material constant in this work. The following equation is employed for surface tension based on the surface tension coefficient of the metal at liquidus temperature $\sigma_l$

$$\sigma = \begin{cases} \dfrac{\sigma_l}{1 + \text{erf}2}\left[1 + \text{erf}\left(\dfrac{4}{T_l - T_s}\left(T - \dfrac{T_l + T_s}{2}\right)\right)\right] & T \leq T_l \\ \sigma_l + \dfrac{\partial\sigma}{\partial T}T & T > T_l \end{cases} \tag{9}$$

The last four terms on the RHS of the momentum equation in Eq. (8) represent the Darcy's effects, surface tension, recoil pressure and Marangoni's flow, respectively. During the laser melting process, those partially melted powders are considered as a mushy region with energy dissipation, which is described by the Darcy's term [132,133]. When the temperature of the metal surface in the melt pool reaches the boiling temperature, evaporation will occur, which results in a recoil pressure on the metal surface, commonly observed as the keyhole phenomena [111]. The Marangoni's flow shows an effect of difference in surface tension due to the temperature gradient in the melt pool and its direction is parallel to the tangential direction of the melt flow surface [63]. These terms are essential to simulate the evolution of various defects and reveal its mechanism.

The melt flow and ambient gas in this simulation are assumed to be incompressible and their continuity equation can be written as:

$$\nabla \cdot \mathbf{u}_f = 0 \tag{10}$$

The temperature equation of the melting process is derived from the energy conservation, given by [108]

$$\begin{aligned} \frac{\partial}{\partial t}(C\rho_T T) + \nabla \cdot (C\rho_T \mathbf{u}_f T) = {}& S_1 + \nabla \cdot \nabla(kT) + \mu_T\left(\nabla\mathbf{u}_f + \mathbf{u}_f\nabla\right) : \nabla\mathbf{u}_f \\ & - L_f\left[\frac{\partial}{\partial t}(\rho_T\alpha_m) + \nabla \cdot (\rho_T\mathbf{u}_f\alpha_m)\right] \\ & - h_c(T - T_{ref})\left|\nabla\alpha'\right|\frac{2C\rho_T}{(C_1\rho_1 + C_2\rho_2)} \\ & - \sigma_{sb}\left(T^4 - T_{ref}^4\right)\left|\nabla\alpha'\right|\frac{2C\rho_T}{(C_1\rho_1 + C_2\rho_2)} \\ & - 0.82\frac{L_v \cdot M \cdot p_0}{(2\pi MRT)^{0.5}}\exp\left(L_v \cdot M\frac{T - T_{LV}}{RTT_{LV}}\right)\left|\nabla\alpha'\right|\frac{2C\rho_T}{(C_1\rho_1 + C_2\rho_2)} \end{aligned} \tag{11}$$

where $S_1$ is the laser input, $\alpha' = (\alpha_1 + 1 - \varepsilon_p)$, $L_f$ is the latent heat of fusion, $h_c$ is the convective heat transfer coefficient, $T_{ref}$ is the reference temperature, and $\sigma_{sb}$ is the Stefan–Boltzmann constant. $2C\rho_T/(C_1\rho_1 + C_2\rho_2)$ represents a sharp surface force term to smear out between two phases [108,131].

The last six terms [52] in Eq. (11) represent the heat transfer due to conduction, dissipation, fusion, convection, radiation, and evaporation. The laser source term $S_1$ can be written as

$$\begin{cases} S_1 = \dfrac{f_1}{\Delta L}Q_{1,s} \\ f_1 = \alpha'\left(e^{-\gamma z_1} - e^{-\gamma z_2}\right) \\ Q_{1,s} = \dfrac{2P}{\pi\left(R_0^2 + \left[\frac{\lambda}{\pi R_0}(z - z_f)\right]^2\right)}\exp\left[\dfrac{-2\left[(x - X_1(t))^2 + (y - Y_1(t))^2\right]}{R_0^2 + \left[\frac{\lambda}{\pi R_0}(z - z_f)\right]^2}\right] \end{cases} \tag{12}$$

where $f_1$ is the laser absorption coefficient based on the general Beer–Lambert form [134], which reflects an exponential decay through the powder bed [135,136]. $z_1$ and $z_2$ are the depths from top to bottom side of the cell under consideration in the powder layer, $\gamma_1$ is the attenuation coefficient, $P$ is the laser power, $R_0$ is the laser beam radius, $z_f$ is the z-coordinate of the lens focus, $\lambda$ is the wave length of the laser, $(x, y, z)$ is the coordinate of the cell, and $(X_1(t), Y_1(t))$ represents the center of the scanning path in the x–y plane.

There have been various models proposed for calculating the absorption coefficient [52,108,131], but they rarely consider the reflection and transmission of the laser. In this study, the penetration of the laser into powder layers is considered, and the absorption model is further divided into two parts depending on whether the metal powders

are fully melted. Experimental results [135] show that the penetration of laser beam into the powder layer is only active prior to complete melting, after which the absorption will be confined to the surface of highly reflective molten pool, as the attenuation coefficients of powders are much (e.g. four orders of magnitude) lower than for bulk metal [137], e.g., iron and copper.

If metallic powders are not melted, the initial attenuation coefficient $\gamma_1$ in the absorption coefficient is determined based on the experiment given by McVey [135]. When metallic powders begin to melt, the molten flow can be easily heated over the boiling point [98], such that it is assumed that the surface of molten pool will absorb most of the laser energy if the liquidus metal begins to evaporate. Existing absorption coefficient models [52,108,131] have assumed only the upper two or three cell layers (interface) of the metal phase absorb the laser energy. In this work, the upper four cell layers of the metal is assumed to absorb most (99%) of the laser energy when reaching the full melting (i.e., $\left(1 - e^{-\gamma_2 \cdot 4\Delta L}\right) = 0.99$), such that the value of $\gamma_2$ can be readily obtained. The attenuation coefficient between these two conditions is approximated using a Gaussian error function,

$$\gamma = \gamma_1 + \frac{\gamma_2 - \gamma_1}{2} \left[ 1 + \mathrm{erf} \left( \frac{4}{T_{\mathrm{LV}} - T_{\mathrm{l}}} \left( T - \frac{T_{\mathrm{LV}} + T_{\mathrm{l}}}{2} \right) \right) \right] \tag{13}$$

The temperature field will be updated after solving Eq. (11). If the temperature of one cell in one particle is higher than the liquidus temperature, this particle will be deleted in the DEM and replaced by spherical fluid cell with a high solidus viscosity $\mu_{\mathrm{s}}$ in the CFD. The solidus viscosity will decrease to liquidus viscosity $\mu_{\mathrm{l}}$ when the temperature reaches the liquidus point. Among studies [52,131,138] that approximate the viscosity transition from the solidus temperature to liquidus temperature, the one proposed by Wang [52] provides an upper and lower limits for the viscosity

$$\ln \mu = \frac{1}{2} \mathrm{erfc} \left[ \frac{4}{\ln T_{\mathrm{l}} - \ln T_{\mathrm{s}}} \cdot \left( \ln T - \frac{\ln T_{\mathrm{l}} + \ln T_{\mathrm{s}}}{2} \right) \right] \cdot (\ln \mu_{\mathrm{s}} - \ln \mu_{\mathrm{l}}) + \ln \mu_{\mathrm{l}} \tag{14}$$

where $\mu_{\mathrm{s}}$ and $\mu_{\mathrm{l}}$ are the viscosities at solidus temperature and liquidus temperature, erfc is the complementary Gaussian error function.

## 2.3. Solution procedure for semi-coupled resolved CFD-DEM

The proposed semi-coupled resolved CFD–DEM approach for SLM has been implemented in two open source codes OpenFoam and LIGGGHTS with the help of a coupling engine *CFDEM* [139,140]. In the coupling, the IB method is combined with the Pressure Implicit with Splitting of Operators (PISO), a standard pressure correction approach for coupling velocity and pressure in CFD simulation [141]. The PISO algorithm consists of one predictor step, where the pressure at the latest timestep is used to calculate the intermediate velocity, and of further corrector steps, where the intermediate and final velocity and pressure fields are obtained iteratively [142]. In the PISO Immersed Boundary (PISO-IB) scheme, the IB method is implemented into the standard PISO scheme to iterate over the continuous forcing term added to the momentum equation that drives the motion of the immersed body. Validation of the scheme can be found from various early test cases [143]. The PISO-IB scheme employed here is based on the one modified by Hager [144].

The following summarizes the complete solution procedure for the proposed semi-coupled resolved CFD–DEM in conjunction with the PISO-IB scheme:

(1) Initialize CFD and DEM domains for the temperature field, pressure field, the velocity field of fluids and the velocity, position of powder particles;

(2) Calculate the drag force acting on the particles in Eq. (5) and update the particle motion using the Newton's Second Law of Motion with a particle collision model in Eq. (1) [145], verify the temperature of each cell in the particle domain and remove a particle from the DEM if the temperature of any of its cells is higher than the solidus temperature and meets the partial melting criterion.

(3) Examine the change of void fraction field to identify whether the particle has been deleted and replace the deleted particles by fluid cells with identical temperature, and update all related parameters in Eq. (7) according to the new volume fraction field and temperature field, including density, heat capacity, thermal conductivity and viscosity.

(4) Calculate the laser source coefficient in Eqs. (12) and (13) based on the position of particles and fluids and the temperature field and update the temperature field based on the temperature equation (11) in CFD that considers the laser source, three heat transfer terms including conduction, convection and radiation, and the enthalpy change due to fusion and evaporation.

(5) Calculate the volume fraction of the metal and protective gas and reconstruct the surface of melt flow using the iso-Advector scheme, a sharp VOF-based interface capturing method, and then update all related parameters in Eq. (7) according to the new volume fraction field and temperature field.

(6) Update the velocity field $\mathbf{u}_f$ and pressure field $p_0$ by solving the Navier–Stokes equation (8) over the whole domain, where the existence of particles is neglected but the buoyancy force, Darcy's effects, surface tension, Marangoni's flow, and recoil pressure are considered instead.

(7) Calculate the drag force exerted on the particles based on the evaluation of $\mathbf{u}_f$ and $p_0$ in Eq. (5) and solve DEM for particle motion in Eq. (1).

(8) Correct the old velocity field into the new velocity field $\mathbf{u}$ in two steps: (a) Calculate $\mathbf{u}_0$ by correcting the old velocity field in the particle domain ($\mathbf{u}_0 = \mathbf{v}_p$) and the interface ($\mathbf{u}_0 = (1 - \varepsilon_p)(\mathbf{v}_p + \boldsymbol{\omega}_p \times \mathbf{r})$) and $\varepsilon_p$ is the void fraction, $\mathbf{r}$ is the position vector of the particle). (b) Further correct the velocity field $\mathbf{u}_0$ according to $\mathbf{u} = \mathbf{u}_0 - \nabla\phi$, where $\nabla^2 \cdot \phi = \nabla \cdot \mathbf{u}_0$ to satisfy the mass conservation under the hypothesis of incompressibility, and then update the pressure $p_0$ using $p = p_0 + \rho \cdot \nabla\phi/\Delta t$.

(9) Go to step (6) to repeat the PISO loop until the residual error or the cycle number reaches the prescribed threshold.

(10) Go to step (1) to repeat the entire simulation until reaching the final time step.

## 3. Simulation of SLM: Results and discussion

### 3.1. Model setup and parameter selection

This study takes the melting process of a typical titanium alloy Ti-6Al-4V powder as an example for the proposed numerical approach. Relevant physical parameters [131] adopted for the modeling are shown in Table 3.

It is physically more realistic to use temperature-dependent thermal parameters [52] for the considered metallic powder. Following American Society for Metals (ASM) [146], the following temperature dependent density $\rho_1$, heat capacity $C_1$, and thermal conductivity $k_1$ of Ti-6Al-4V alloy are adopted

$$
\begin{cases}
\rho_1(\text{kg/m}^3) = \begin{cases} 4420 & T < 1268\text{K} \\ 4420 - 0.154(T - 298) & 1268\text{K} < T < 1923\text{K} \\ 3920 - 0.680(T - 1923) & T \geq 1923\text{K} \end{cases} \\[2em]
C_1(\text{m}^2/(\text{s}^2\ \text{K})) = \begin{cases} 411.5 & T < 1268\text{K} \\ 411.5 + 0.2T + 5 \times 10^{-7}T^2 & 1268\text{K} < T < 1923\text{K} \\ 830 & T \geq 1923\text{K} \end{cases} \\[2em]
k_1(\text{kg m}/(\text{s}^3\ \text{K})) = \begin{cases} 19.0 & T < 1268\text{K} \\ -0.797 + 0.0182T - 2 \times 10^{-6}T^2 & 1268\text{K} < T < 1923\text{K} \\ 33.4 & 1923\text{K} < T < 1973\text{K} \\ 34.6 & T \geq 1973\text{K} \end{cases}
\end{cases}
\tag{15}
$$

The chosen viscosity at solidus temperature $\mu_s$ is crucial for the accuracy of simulation results. A high viscosity may help to ensure the movement of those fluids close to that of the solid powders and hence a much larger Deborah Number than 1 [147]. Experimental data [148] show that the viscosity $\mu_s$ of Ti-6Al-4V alloy is larger than $10^{7.5}$ Pa s at low strain rate ($<10$ s$^{-1}$), which is nearly $6 \times 10^9$ times larger than the viscosity at melt point $\mu_l$ (0.005 Pa s). However, such a large viscosity at solidus temperature $\mu_s$ requires extremely large number of PISO correction iterations to achieve the phase fraction and pressure convergence [149]. To fetch a balance between efficiency and accuracy, a relatively small viscosity is adopted in this study as $\mu_s = 0.005\sqrt[4]{10^{7.5}/0.005} = 1.41$ Pa · s, which can guarantee that the Deborah Number is much larger than 1 and the required number of iterations can drop to a reasonable level to reduce computational cost [150].

The grain size distribution of powders in the simulations is ranged from 9 μm to 28 μm (shown in Fig. 1a), following the powder size distribution of Ti-6Al-4V measured by Panwisawas [108]. The mean diameter is measured

**Table 3**

Physical parameters of the numerical model.

| Parameter | Value and units | Parameter | Value and units |
|---|---|---|---|
| Liquidus temperature | $T_l = 1923$ K | Solidus temperature | $T_s = 1878$ K |
| Boiling temperature | $T_{LV} = 3133$ K | Initial temperature | $T_0 = 300$ K |
| Laser Diameter | $D_L = 140$ μm | Laser velocity | $v_L = 60$ cm/s |
| Atmospheric pressure | $p_0 = 101\,000$ Pa | Molar mass | $M = 446.07$ g/mol |
| Viscosity of air | $\mu_2 = 1.5 \times 10^{-5}$ m$^2$/s | Heat capacity of air | $C_2 = 1164$ m$^2$/s$^2$ K |
| Latent heat of fusion | $L_f = 2.88 \times 10^5$ m$^2$/s$^2$ | Air density | $\rho_2 = 1$ kg/m$^3$ |
| Latent heat of evaporation | $L_V = 4.7 \times 10^6$ m$^2$/s$^2$ | Viscosity of liquidTi-6Al-4V alloy | $\mu_1 = 0.005$ Pa s |
| Initial attenuation coefficient | $\gamma_1 = 0.0144$ | Surface tension coefficient at melt point | $\sigma_1 = 1.5$ kg/s$^2$ |
| Change rate of surface tension coefficient | $\frac{\partial \sigma}{\partial T} = -2.6 \times 10^{-4}$ kg/(s$^2$ K) | Convective heat transfer coefficient | h = 19 kg s$^3$ K |

**Table 4**

Model properties and computational domain of four cases.

| Type | Property | CFD Domain | DEM Domain |
|---|---|---|---|
| Convergence study (Single track) | 5 μm–200 W − Gaussian<br>4 μm–200 W − Gaussian<br>3.5 μm–200 W − Gaussian | L = 600 μm<br>W = 320 μm<br>H = 220 μm | L = 720 μm<br>W = 400 μm<br>H = 300 μm |
| Validation test (Single track) | 4 μm–300 W − Gaussian<br>4 μm–150 W − Gaussian<br>4 μm–200 W − Uniform | L = 720 μm<br>W = 400 μm<br>H = 220 μm | L = 1000 μm<br>W = 500 μm<br>H = 300 μm |
| Validation test (Multiple tracks) | 4 μm–200 W-Gaussian<br>Hatch distance $= 1.25D_L$<br>4 μm–200 W-Gaussian<br>Hatch distance $= D_L$<br>4 μm–200 W-Gaussian<br>Hatch distance $= 0.75D_L$ | L = 720 μm<br>W = 576 μm<br>H = 220 μm<br>L = 720 μm<br>W = 512 μm<br>H = 220 μm | L = 1000 μm<br>W = 680 μm<br>H = 300 μm<br>L = 1000 μm<br>W = 620 μm<br>H = 300 μm |
| Multi-layer model (Single track) | 4 μm-200 W-Gaussian | L = 640 μm<br>W = 400 μm<br>H = 320 μm | L = 900 μm<br>W = 500 μm<br>H = 300 μm |

around 36 μm, nine times of the length of grid size (4 μm) used in the CFD domain. Fig. 1(b) presents the model setup for the subsequent convergence study, validation and multi-layer simulations. A smaller CFD domain compared to that of the DEM is adopted to reduce the computational cost. Table 4 summarizes the model properties used in the following simulations, including the grid size, laser beam and simulation domain. As for the naming of laser beam indicated in the table, 4 μm-200 W-Gaussian means that the grid size is 4 μm and the laser energy is 200 W with a Gaussian distribution. In addition to convergence and validation studies, we will also present a multi-layer simulation where both the layering process and the melting process are modeled. During the layering process, the standby powders are compressed within the work area by a roller a radius of 1000 μm and height of 500 μm to form a new layer preparing for melting.

A substrate of 80 μm in thickness is considered and is overlaid by a powder bed 100 μm thick. The time step of CFD is set to be $1 \times 10^{-7}$ s, ten times of that for the DEM ($1 \times 10^{-8}$ s). The bottom boundary is set as a non-slip wall and zero gradient for both temperature and pressure, and other boundaries are set as fixed value for pressure and zero gradient for velocity and temperature.

### 3.2. Convergence study

A convergence study is performed to determine a proper grid size for the validation model that offers balanced efficiency and accuracy for the computation. Previous numerical experience on unresolved coupled CFD–DEM studies indicates the accuracy of simulation results can be guaranteed if the particle size is 8 times larger than the grid size [123]. With a mean diameter of powders of 36 μm, three cases of CFD grid sizes (5 μm, 4 μm and 3.5 μm) are considered. The top view of the simulation result for the case of grid size 4 μm is shown in Fig. 2(a),
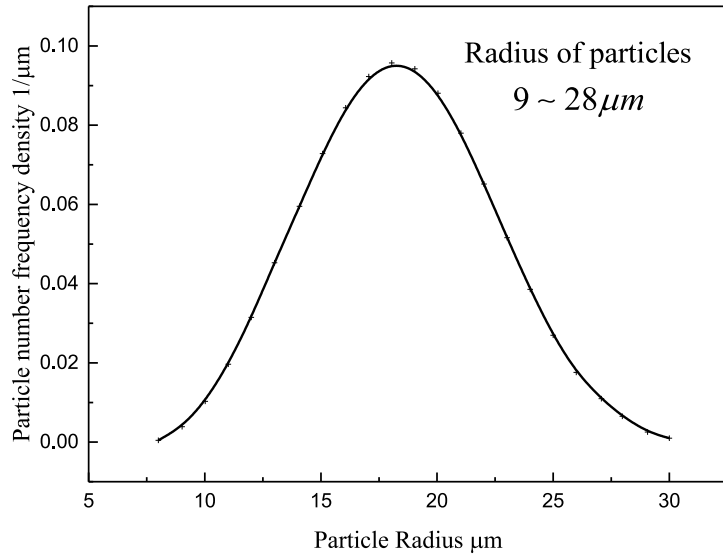
(a) Particle size distribution adopted for Ti-6Al-4V alloy powder
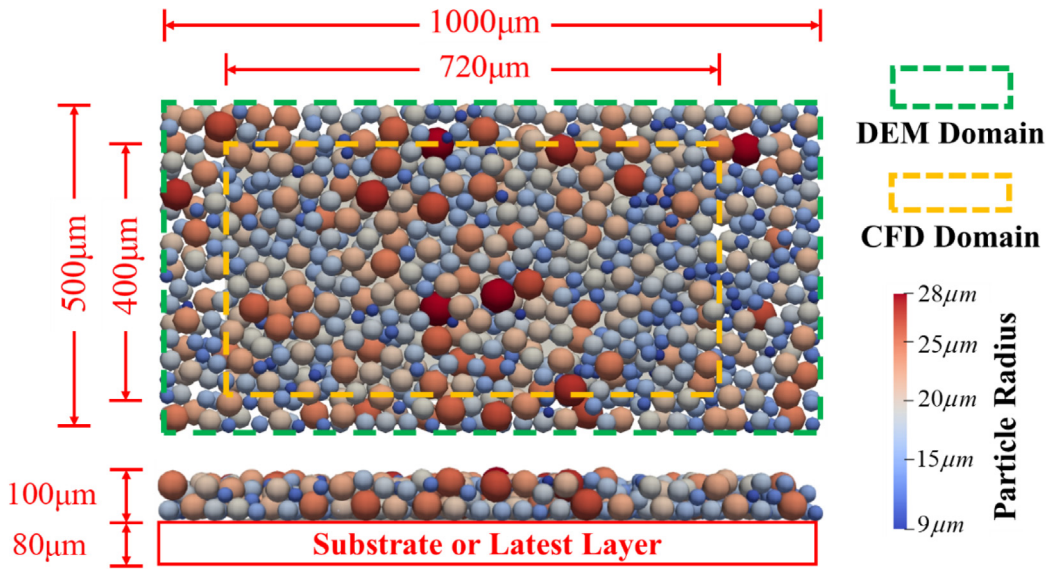


(b) Powder bed and simulation domain

**Fig. 1.** Model setup for coupled CFD–DEM simulation of SLM of Ti-6Al-4V alloy powder.

and the longitudinal section A–A at y = 160 μm and the cross section B–B at x = 300 μm are chosen, as shown in Fig. 2(b) and (c).

Fig. 3 shows a comparison of the longitudinal and transverse cross section contours of the molten track with different grid sizes where contours in black, red and blue represent grid size cases of 5 μm, 4 μm and 3.5 μm, respectively. Particular attention is paid to the longitudinal section A–A of the molten track behind the laser spot from x = 100 μm to x = 400 μm and the cross-section B–B ranges from y = 50 μm to y = 320 μm. Evidently, similar contours are observed at the three cases of grid size. The maximum difference between the black and red
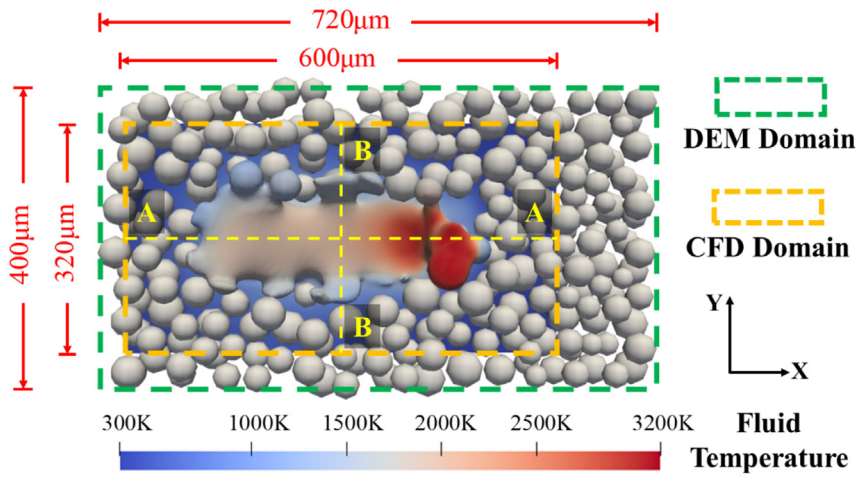
(a)    Top view of simulation result with grid size 4 μm
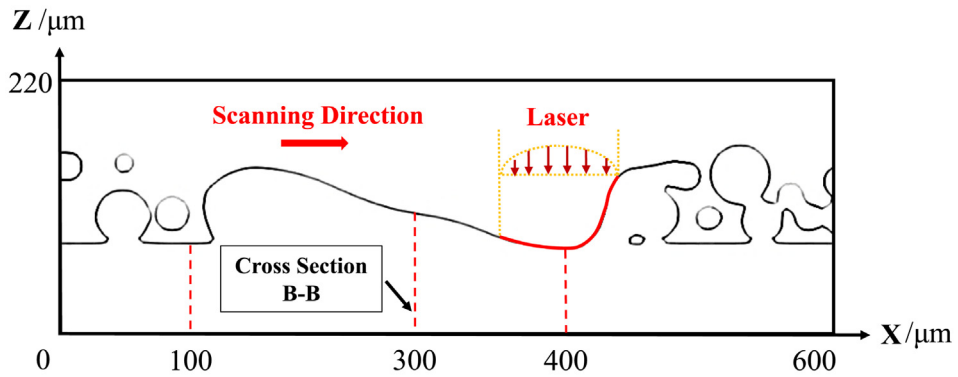


(b) Longitudinal section A-A contour
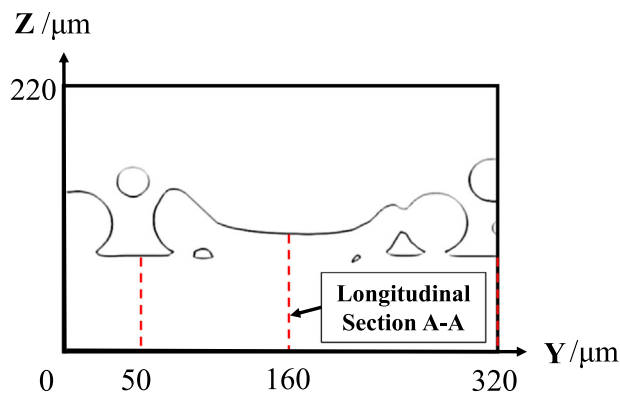


(c) Cross section B-B contour

**Fig. 2.** Top view and cross section contours of the molten track with CFD grid size 4 μm.
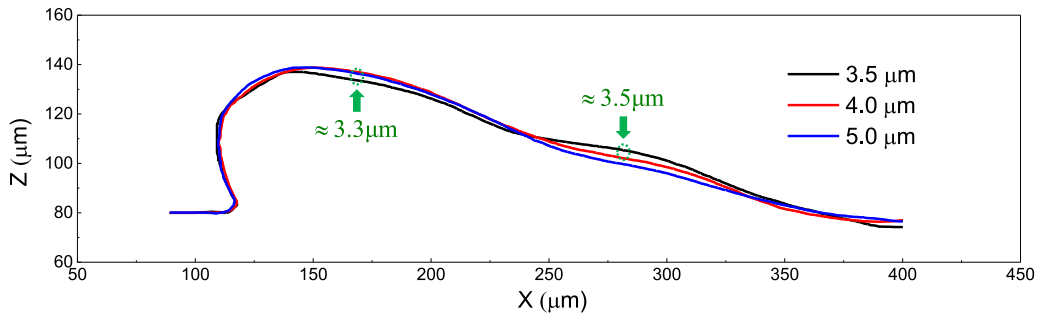
(a) Longitudinal section at longitudinal section A-A
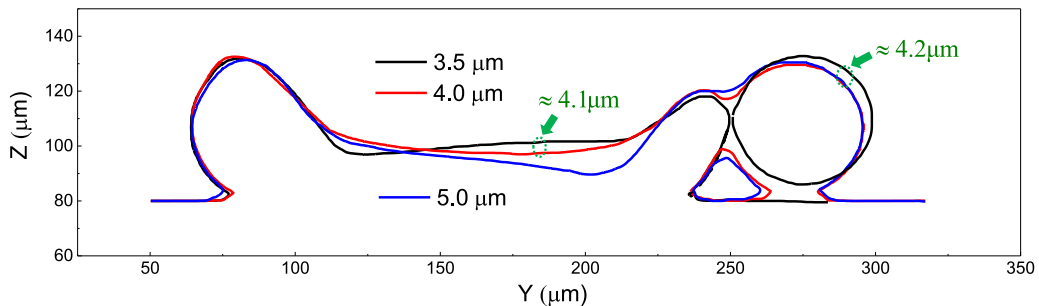


(b) Transverse cross section at cross section B-B

**Fig. 3.** Cross section contours of the molten track with three grid sizes.

contours is about 4 μm, which only mildly changes the curvature of the molten track surface rather than the whole structure.

Fig. 4 further shows the temperature profile of the same longitudinal section A–A contour, from x = 110 μm to x = 400 μm in x direction. The black and red contours are well overlapped except in the region from x = 300 μm to x = 375 μm due to the high temperature and difference in cross section B–B contours. Note that the absorption coefficient is also related to the grid size. However, since the maximum temperature difference is only about 130 K, which is around 5% of the temperature at that point, the difference between the cross-section contours from x = 150 μm to x = 200 μm does not result in an appreciable temperature difference due to the solidification. In the rest of this paper, a grid size of 4 μm of CFD is adopted to balance the accuracy and efficiency.

### 3.3. Validation of model predictions against experimental data

The multiscale predictions of SLM based on the semi-coupled resolved CFD–DEM are further validated by experimental data in this subsection. Specifically, three validation cases with varying laser power, laser energy distribution, and hatch distance of multiple tracks are considered.

Fig. 5 shows the Marangoni driven ripples and piled track-heads captured by our multiscale approach in comparison with observations from experiments [151]. Marangoni effect is typical flow instability observed in SLM, caused by high fluid temperature gradient that induces changes in surface tension. As the surface tension decreases with increasing temperature for Ti-6Al-4V alloy, the low temperature molten flow behind the laser spot has a higher surface tension which drives the molten pool flowing back to form the ripples during quick solidification. In this simulation, the scanning speed is 60 cm/s and three laser powers, 150 W, 200 W and 300 W, are tried. When the laser power grows stronger, the ripples become larger in size and sharper, due primarily to larger molten pool and higher temperature gradient caused. Increasing laser power may lead to initially dense but later sparser ripples. When the laser power is low, the energy may not be sufficient to form ripples in some regions. However, if the laser
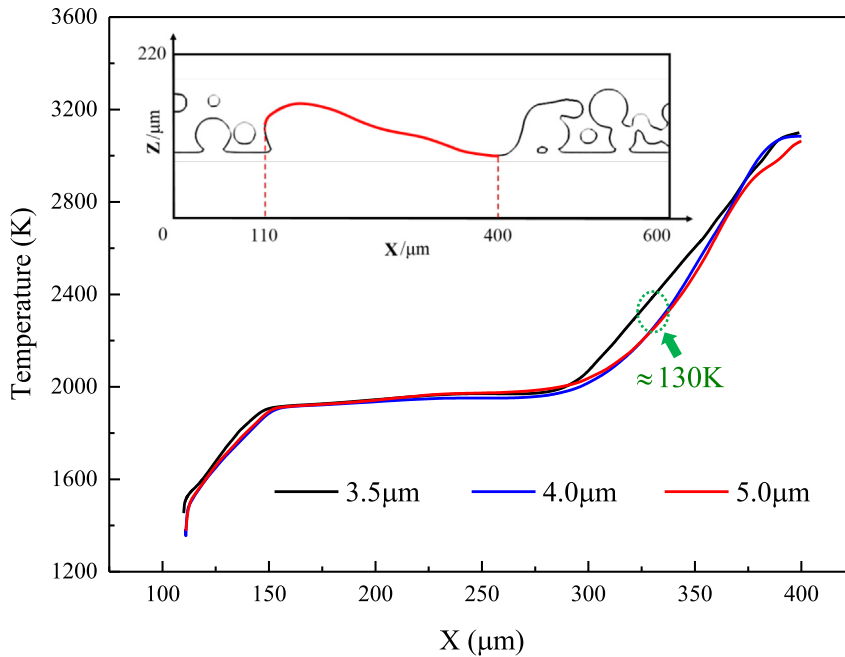
**Fig. 4.** Temperature profiles along longitudinal section A–A with different grid sizes.

power is adequately high, relatively larger molten pool, higher temperature gradient and recoil force may combine to result in closer ripples, increased thickness, size and interval of final ripples. These phenomenon are consistent with the experimental observations [151] shown in Fig. 5(d).

The distribution of laser energy during the melting process can also affect the formation of ripples and the surface quality of molten track. Experimental results [34] have confirmed that the molten track formed by a uniform distributed laser energy is more regular and flatter compared to a Gaussian distributed one. A comparison of the numerical predictions by the Gaussian and uniform distribution types of laser energy is presented in Fig. 6 at a laser power of 200 W. In the figure, the viscosity contour features a red subregion representing the solidus viscosity and a blue one for the liquidus viscosity. The latter is also commonly called molten pool. A further comparison of the molten pool with the ripples in Fig. 6(a) shows that the two are highly coincident with each other, confirming that the ripples is indeed dominated by the molten pool. Since the Gaussian distribution of laser energy has its energy concentrated at the laser center, it is reasonable to find that higher temperature gradient and sharper ripples are observed as compared to the uniform laser energy distribution case.

The roughness of the molten track is one of the important indices for quality control of SLM. It is evaluated in this study using a commonly used one-dimensional roughness parameter, the arithmetic average roughness $Ra$. Three longitudinal sections (Fig. 6(a)) of the solidified molten track, at y = 150 μm (section C–C), y = 200 μm (section D–D) and y = 250 μm (section E–E), respectively, are chosen to calculate the corresponding average thickness $d_{\mathrm{m}}$ and average roughness $Ra$ (Fig. 7). The longitudinal section D–D refers to the center line of the molten track wherein $Ra$ is smaller when the laser power is 300 W which can provide sufficient energy to have the powders fully melted. Pores may be generated at the bottom of the powder bed with a low laser energy, such as the case of laser energy at 200 W. It should be noted that the two polylines in the case of Gaussian distribution laser energy present a 'V' shape because the laser energy is primarily concentrated at the center of molten track, leading to less energy and insufficient melting and thus a rough surface along the track edge. It can be concluded that the surface of the molten track is flatter and smaller surface roughness when subjected to a uniform laser energy distribution.

By virtue of the coupled CFD–DEM formulation, the powder movement during the melting process can also be captured, which has not been attempted by existing studies. Critical in driving the powder movement during the melting process are the vapor recoil and the spatially varying absorptivity [152], which may cause localized fluid flow and further interactions with surrounding powders [98]. The interactions between melt flow and surrounding
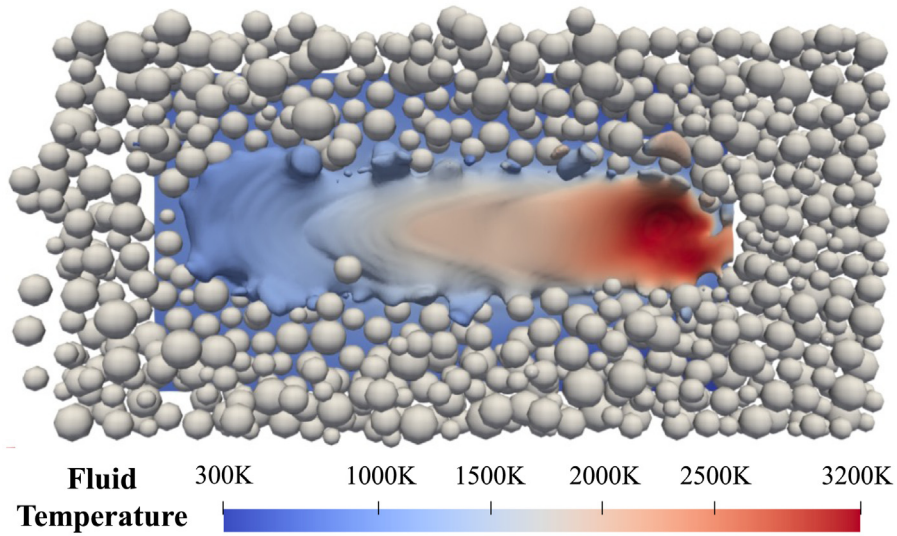
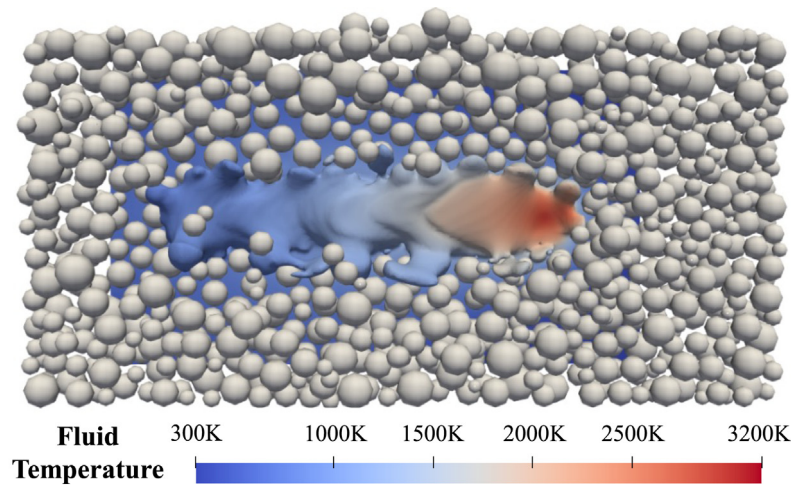**(a)** Simulation result of temperature field with laser power $P = 300$ W
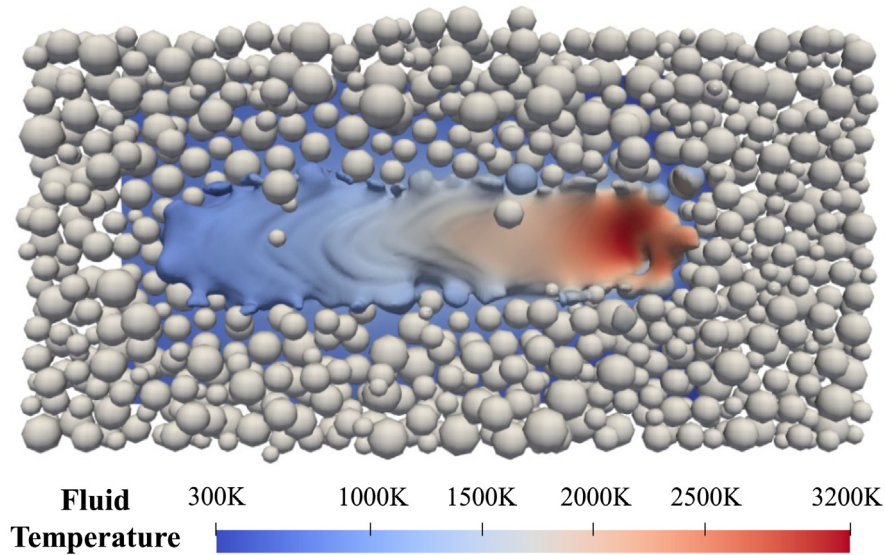


**(b)** Simulation result of temperature field with laser power $P = 200$ W

**Fig. 5.** Comparison of multiscale simulation of SLM with different laser power (a–c) with experimental observations (d).

particles and particle–particle collisions have been captured in our simulation. Fig. 8 shows a qualitative comparison of experimental observations by high speed imaging [98] and our simulation results. In the figure, yellow arrow trajectories represent powders swept away from the molten pool, whereas others indicate powders falling into the molten pool. Note that vapor could serve as a dominant factor [98] not considered for the powder movement in this study. It will be considered in a future work.

The hatch distance is a dominant factor in multi-track SLM, controlling the manufacturing efficiency and surface quality. Fig. 9(a) shows experimental observations of the surface quality of multiple molten tracks [10,153,154] with appreciable discontinuities and sticking particles along the step edges that all contribute to the increase of surface

(c) Simulation result of temperature field with laser power $P = 150$ W
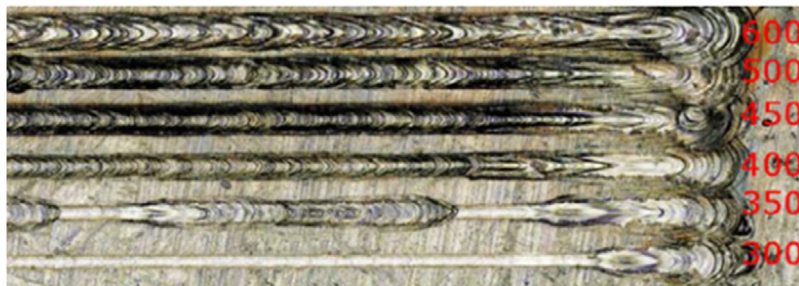


(d) Experimental results by Trappa et al. [151]

**Fig. 5.** (*continued*).

roughness. Note that the discontinuities have been a result of the so-called 'balling effect' or 'Plateau–Rayleigh instability' due to surface tension. This defect can be eliminated using the scanning strategy with overlapped scan tracks, as shown in Fig. 9(b). For example, A 25% scan overlap can effectively remove the discontinuity at the step edge [155], reaching a higher Vickers microhardness value of final samples. Our numerical approach can faithfully reproduce the phenomenon and the remedy. As shown in Fig. 10, three multi-track numerical simulations are performed with a hatch distance at 125%, 100% and 75% of the laser diameter, respectively. Evidently, when the hatch distance is greater than the laser diameter, both sticking particles and discontinuity can be observed (Fig. 10a). Reducing the hatch distance to the same size of laser diameter can help eliminate the sticking particles but discontinuity due to balling effect can be still found (Fig. 10b). With a 25% overlapping, both defects can be effectively reduced (Fig. 10c).

### 3.4. Simulation of multi-layer SLM

SLM is commonly based on a layered manufacturing process where a single layer of molten track is formed from the metallic powders and is bonded to previous layers until the final object is completed [156], as illustrated in Fig. 11. This section further demonstrates the capacity of our proposed method in modeling multi-layer SLM process. The same set of model parameters as listed in Table 4 are used.

We follow four steps to model the preparation for the next powder layer after melting the former layer. (1) Remove the suspended portion (Fig. 12(a)) of the molten track due to the extremely high viscosity and Darcy's
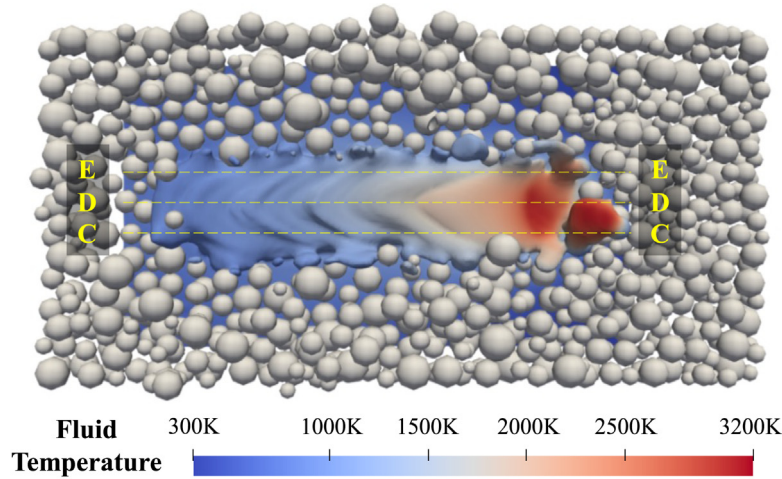
(a) Simulation result of temperature field with uniform laser energy distribution
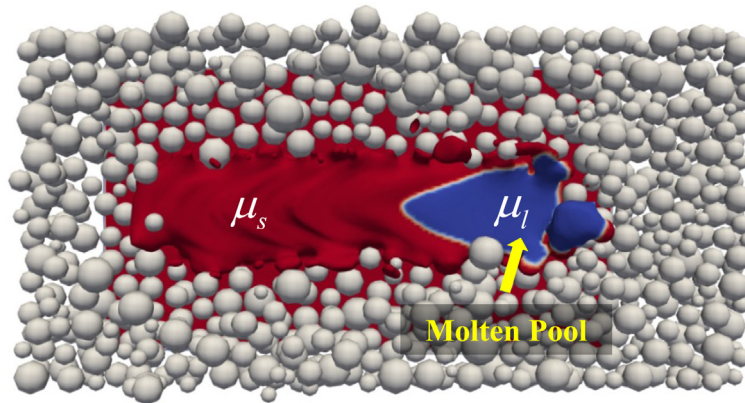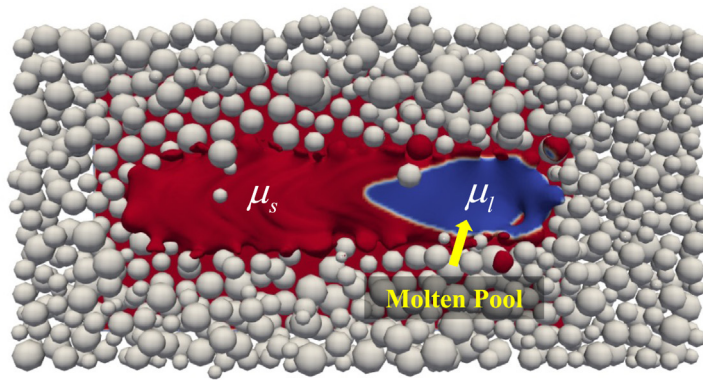


(b) Simulation result of viscosity field with uniform laser energy distribution

**Fig. 6.** Comparison of simulation (a–c) and experiments (d) on the melting by different laser energy distributions.

effects (Fig. 12(b)) that may adversely affect the subsequent layering process. These suspended parts refer to the spatters observed in experiments which would cause the denudation zone if left uncleared [98]. The unresolved CFD–DEM with a large grid size (150 μm) as described in Section 2.1 is used in this step. (a) Replace the molten track in the CFD by fixed particles with the same diameter as the grid size to ensure accurate transformation of complex molten surfaces, as shown in Fig. 12(c). The replacement only applies to cells with a volume fraction$_l$ larger than 0.5 where particles are in the center of cells. In doing so, the interaction between the powders and the solidified metal can be simplified as the collision between particles in the DEM. (3) Perform DEM simulation to bring all moving particles into an static equilibrium state (Fig. 12(d)), and use a roller to press and push the standby particles from the left side to the work area in the fourth step (Fig. 12(d)), finishing the layering process. (4) Apply laser beam and melt this new particle layer. The above four steps are repeated to simulate a multi-layer SLM process to finish a design product.

Significant surface roughness along the edge of multi-layer molten tracks and apparent ripples are found in both our simulation results and SEM images of experimental tests [157] (Fig. 13). The surface roughness is composed of sticking powders, partially melted powders and discontinuities caused by balling effect [155]. It may affect the surface quality and the mechanical properties of the final fabricated product. As shown in Section 3.3, a 25% overlap between two neighboring tracks can help efficiently eliminate this defect. The overlapping strategy, however, may

(c) Simulation result of viscosity field with Gaussian laser energy distribution
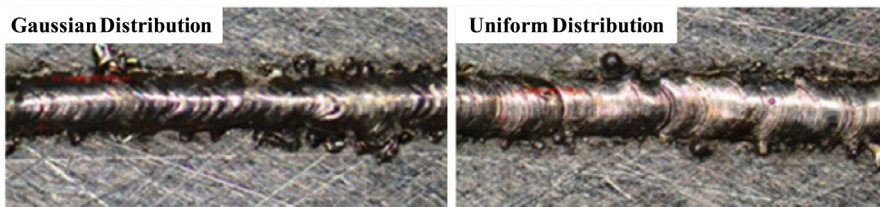


(d) Experimental results by Okunkova et al.[34]
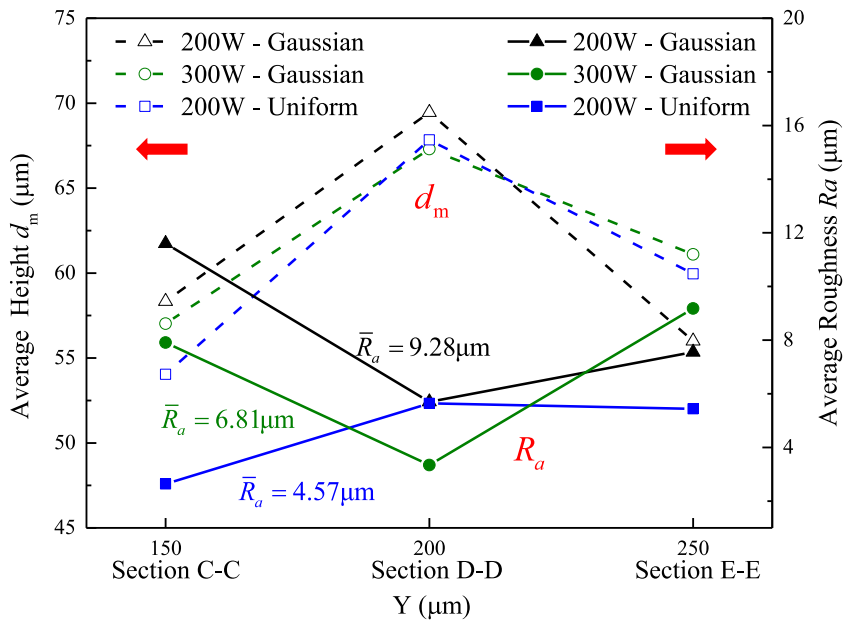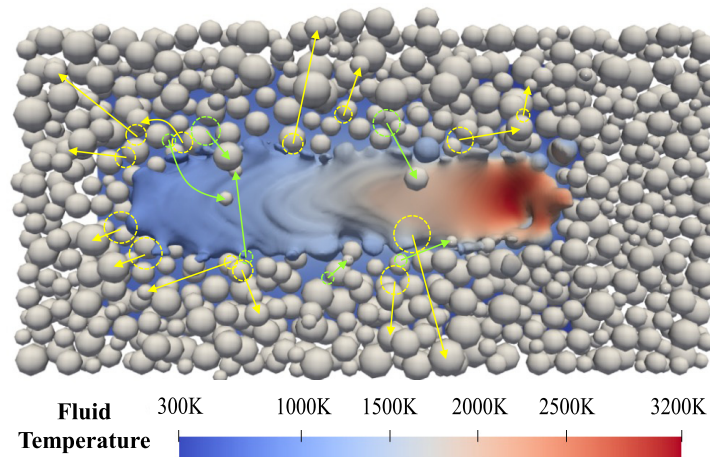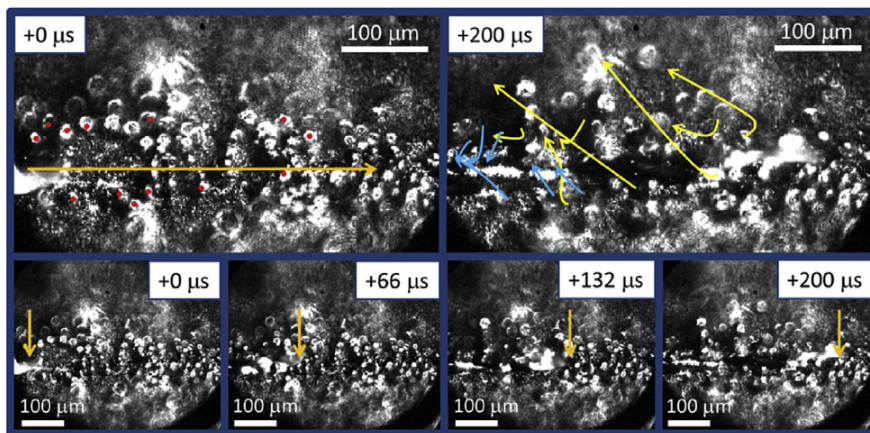
**Fig. 6.** (*continued*).



**Fig. 7.** Simulation results of average height $d_\mathrm{m}$ and average roughness $Ra$.

(a) Simulation result of typical powder movement (200W-Gaussian)



(b) High speed imaging of molten track progression and powder movement[97]

**Fig. 8.** Simulated powder movement during the melting process (a) in comparison with experiments (b).

not work for some special situations, such as the porous implant structure shown in Fig. 13(c), as the working area may be limited in size to allow multiple tracks and significant overlapping and hence this defect may remain in the product. Nevertheless, the proposed approach may serve as a robust analytical tool for systematic parametric study in this case for design of optimal printing strategies.

## 4. Conclusions and outlooks

A semi-coupled resolved CFD–DEM approach has been proposed for solving a class of granular media problems that involve thermal-induced phase changes and particle–fluid interactions. It has been validated by a typical powder-based selective laser melting (SLM) process using titanium alloy Ti-6Al-4V. The influences of laser power, laser energy distribution and hatch distance on the melting quality have been examined. It is demonstrated that the proposed approach is capable of capturing key features and observations found in SLM experiments and its predictions are consistent with existing data. An unresolved CFD–DEM has been further employed to simulate the layering process for preparing the next powder layer after melting of one layer. A combination of the semi-coupled resolved CFD–DEM for the melting process and the unresolved CFD–DEM for the layering process of next particle layer offer a complete cycle of multi-layer simulation framework for powder-based SLM. Major conclusions drawn from the study are summarized as follows:
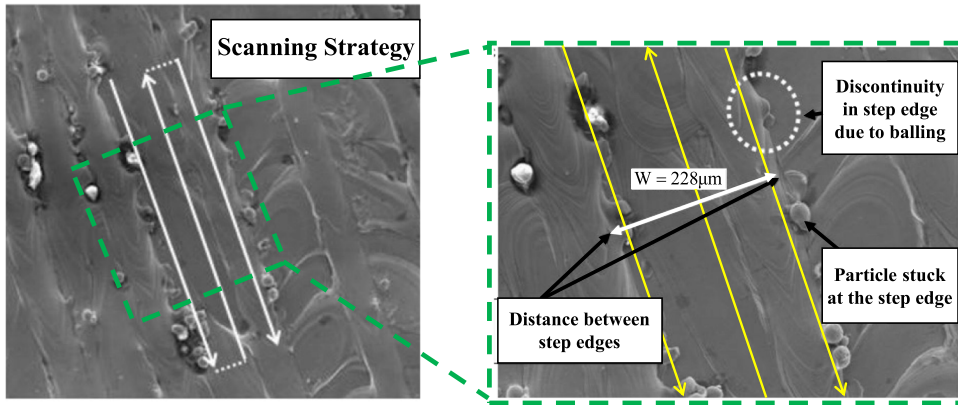
(a) Experimental result of three overlapped scan tracks [10]
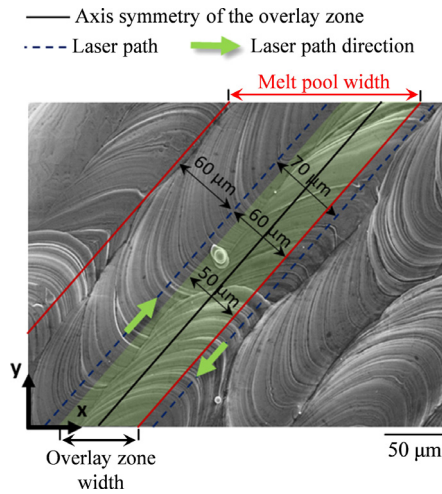


(b) Experimental result of multiple overlapped scan tracks [154].

**Fig. 9.** SEM images of multiple molten tracks observed in experiments (see [154]).

(a) The semi-coupled resolved CFD–DEM method features the employment of Immersed Boundary Method to model the viscous fluids surrounding each solid particle in conjunction with a fictious CFD domain occupying the actual position of particle. It expediates the modeling of heat transfers between the actual fluids and the fictitious particles as a multiphase problem within the CFD, whereas the particle–fluid interactions can be treated by the coupling between DEM and CFD.

(b) A unified coupled CFD–DEM framework combining the semi-coupled resolved CFD–DEM and the unresolved CFD–DEM as described in the study can help effectively reproduce the entire SLM processes, including resolving the motion of powders, dynamics of molten flow, and powder-flow interaction. This framework provides a basic methodological tool for future optimization of powder based SLM over various factors, such as the scanning strategy, initial temperature and deposition method.

(c) Three phases, including the ambient gas, solid metallic powders and molten flow can be fully built in this melting process and rigorously modeled by the semi-coupled resolved CFD–DEM. Key to the success of the proposed method is the integration of the iso-Advector method and the Immersed Boundary Method to resolve accurate molten surfaces and particle–fluid interactions in conjunction with an absorption model to capture the interactions between laser energy penetration and highly reflective molten pool that result in multiple phenomena including the phase change, Marangoni effect, recoil force and Darcy's effects. Simulation results with different laser power, laser energy distribution and hatch distance demonstrate the proposed method can capture crucial
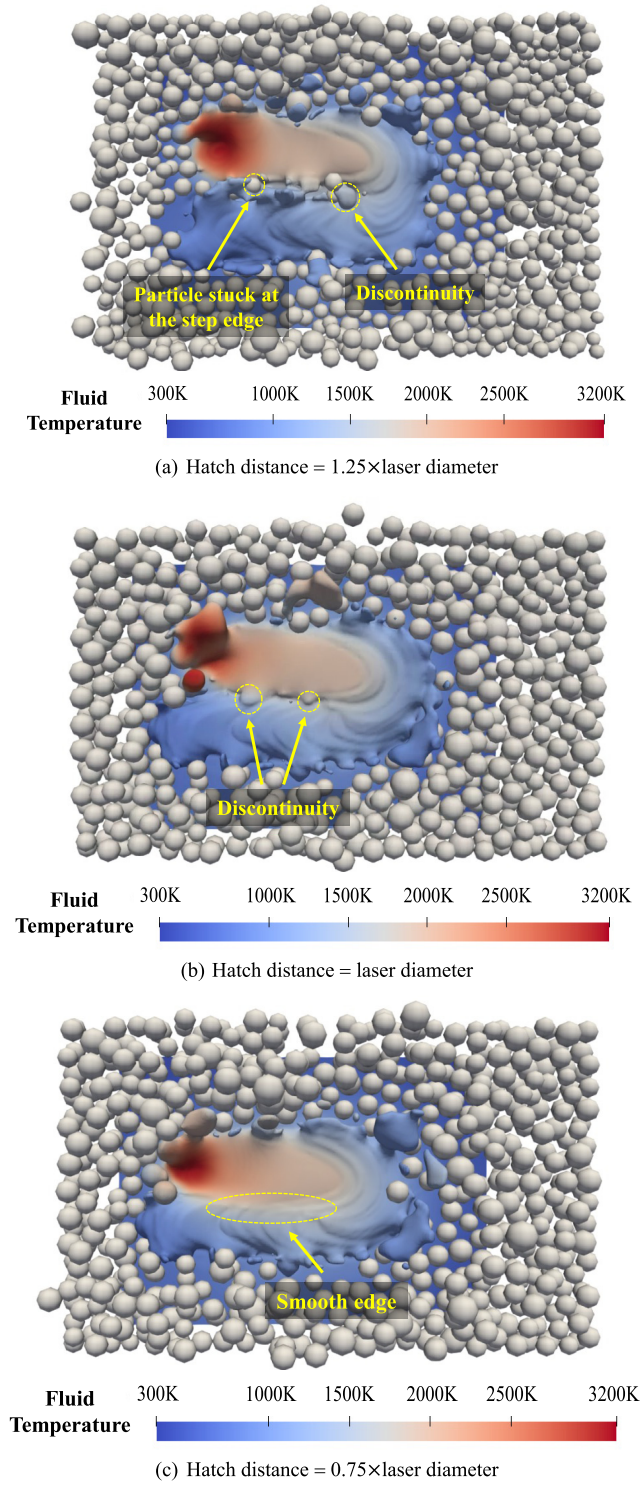
(a) Hatch distance = 1.25×laser diameter



(b) Hatch distance = laser diameter



(c) Hatch distance = 0.75×laser diameter

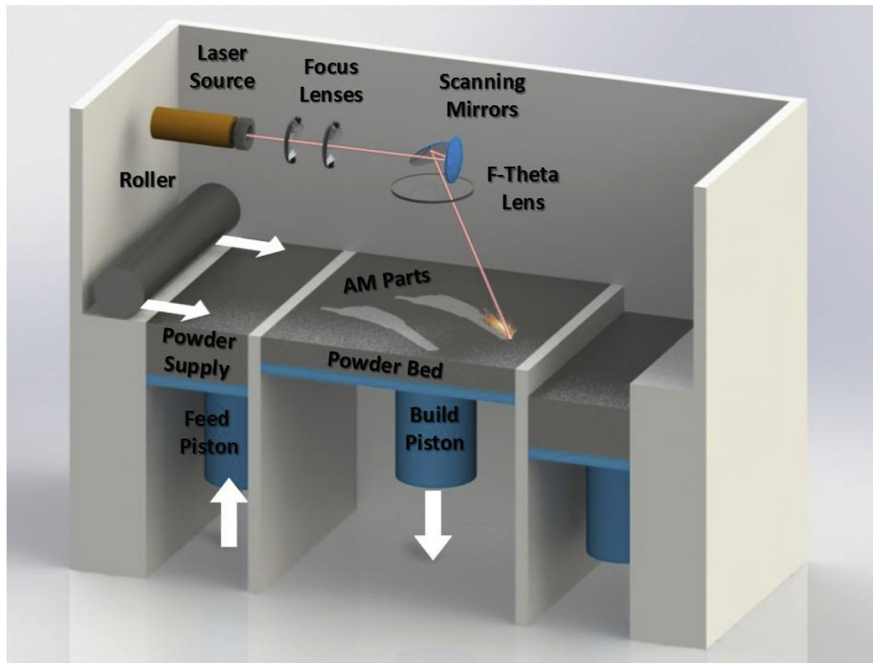**Fig. 10.** Simulation results of multi-track model.

**Fig. 11.** Schematic diagram for SLM [36].

phenomena in SLM observed experimentally, such as typical powder motions, ripples of single molten track and surface characteristics of multiple tracks.

(d) Our study shows that a low laser power source may cause inner pores due to partially melted powders, leading to a rough molten surface. A uniform energy distribution for laser source can produce regular ripples with smaller surface roughness. In examining the multi-track case, a reasonable overlap between two molten tracks is found necessary to improve the surface quality and eliminate possible discontinuity and sticking particles along the track edge. During the melting process, certain particles may collapse and collide into the molten track, while others may be ejected away due to the recoil pressure and Marangoni effect, which may affect neighboring tracks.

(e) Within the developed framework, four steps are proposed to prepare a new powder layer after one melting operation, including the deletion of suspended fluids, replacement of molten track, equilibrium process and powder layering, wherein the replacement and powder layering are a key step. The replacement using small particles with the same diameter as the grid size can maintain the primary characteristic of a complex molten surface while improving the computational efficiency as compared with a fully resolved CFD–DEM. The powder layering process is modeled with an unresolved CFD–DEM in consideration of modeling components including standby powders, roller and container structure.

(f) Our simulation results of multi-layer SLM process and further comparison with SEM image obtained from experiments indicate that balling effect can cause surface roughness along the track edge due to sticking powders, partially melted powders and discontinuities. The surface roughness may accumulate in the thickness direction and influence properties of mechanical behavior of the built part. The proposed approach offers a systematic tool for future parametric studies to eliminate this defect.

The study constitutes a very first step towards more rigorous simulation of powder based SLM and definitely will not be the last. There are various challenges remaining to be addressed. The proposed framework has two major drawbacks to be improved upon: consideration of vapor phase and the related computational cost. Vapor commonly flows at high speed which may cause spattering of fluids and ejection of powders. Further incorporation of vapor flow is indeed required but challenging. It may require much small grid size for a fully resolved CFD–DEM, which may significantly increase the computational cost. More robust numerical strategies need to be developed to effectively
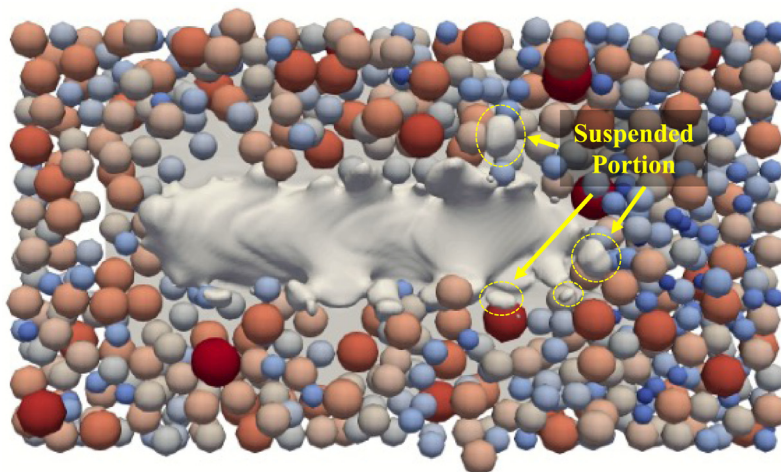
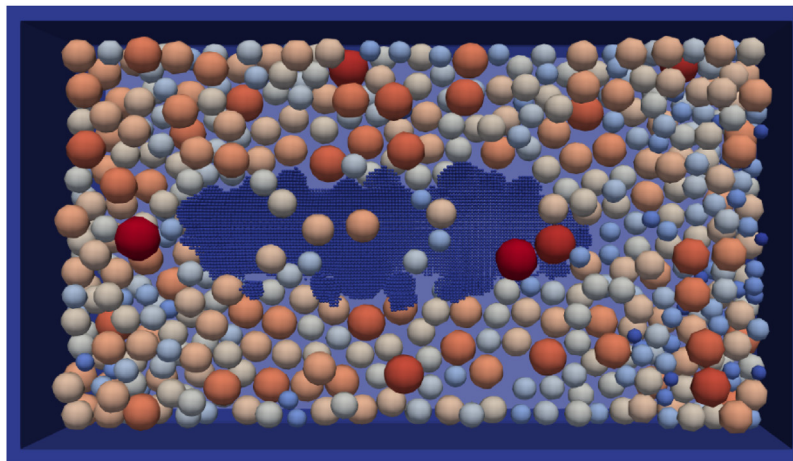(a)  Original molten track with suspended parts
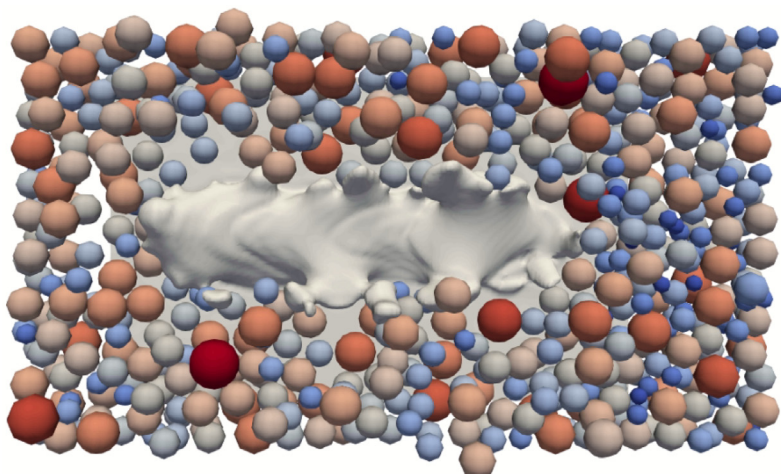


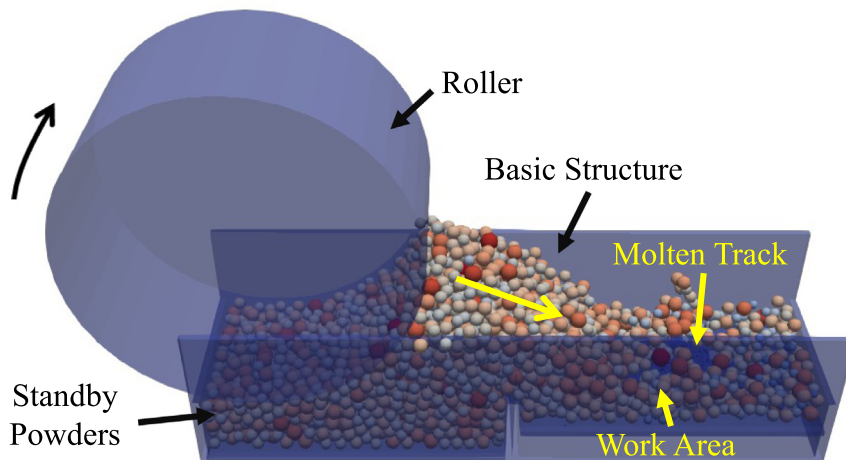(b)  Step one: molten track without suspended parts
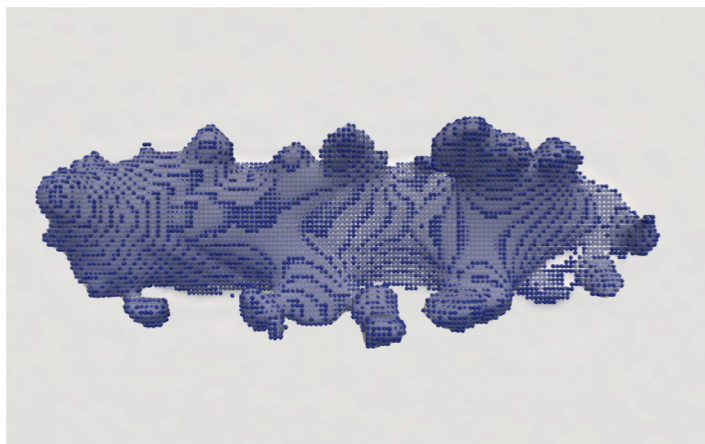


(c)  Step two: replacement of molten track

**Fig. 12.** Steps of preparation for next particle layer for SLM.

(d) Step three: equilibrium state



(e) Step four: deposition process

Fig. 12. (*continued*).

improve the computational efficiency while maintaining accuracy. In addition, more systematic investigations are required, based on a rigorously calibrated semi-coupled resolved CFD–DEM and multiscale model integrated with realistic physical components aforementioned, to identify optimal parameters and formation mechanism of potential defects for economical and optimized design of SLM. Finally, an efficient numerical model with multiple layers and tracks should be developed to enable effective simulation and evaluation of mechanical behavior of SLM products for possible industrial applications.

**Declaration of competing interest**

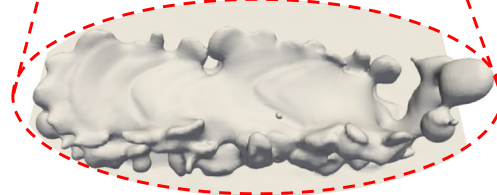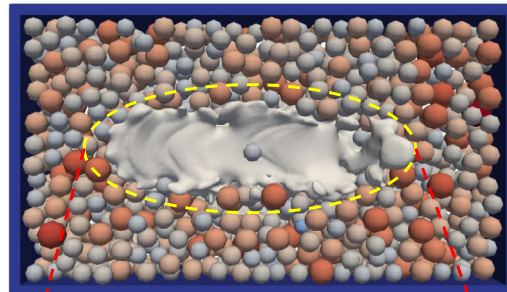The authors declare that they have no known competing financial interests or personal relationships that could have appeared to influence the work reported in this paper.
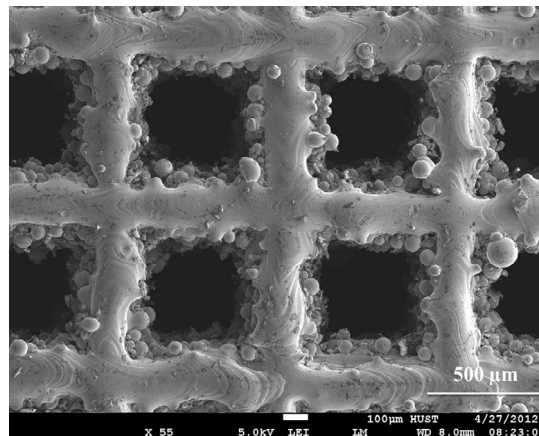
**Acknowledgments**
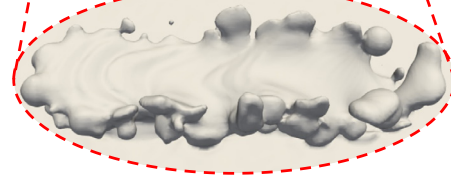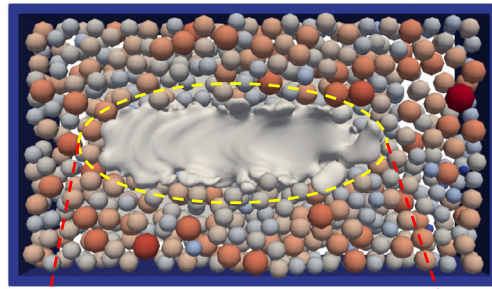
(a) Two-layer model and its molten track



(b) Three-layer model and its molten track



(c) SEM image of the porous Ti-6Al-4V implants[156]

**Fig. 13.** Simulation and experimental results of multi-layer molten tracks.

# References

[1] B. Berman, 3-d printing: The new industrial revolution, Bus. Horiz. 55 (2012) 155–162.

[2] D.L. Bourell, M.C. Leu, D.W. Rosen, Roadmap for Additive Manufacturing: Identifying the Future of Freeform Processing, The University of Texas at Austin, Austin, TX, 2009, pp. 11–15.

[3] S. Srivatsa, Additive Manufacturing (AM) Design and Simulation Tools Study, Final Report, Air Force Research Laboratory, WP AFB OH, 2014.

[4] Y. Yang, Y. Chen, Y. Wei, Y. Li, 3D printing of shape memory polymer for functional part fabrication, Int. J. Adv. Manuf. Technol. 84 (2016) 2079–2095.

[5] A.A. Antonysamy, Microstructure, Texture and Mechanical Property Evolution During AdditiveManufacturing of Ti6Al4V Alloy for Aerospace Applications, The University of Manchester (United Kingdom), 2012.

[6] N. Hoye, H.J. Li, D. Cuiuri, A.M. Paradowska, Measurement of Residual Stresses in Titanium Aerospace Components Formed Via Additive Manufacturing, Trans. Tech. Publ., 2014, pp. 124–129.

[7] S.A. Gowers, V.F. Curto, C.A. Seneci, C. Wang, S. Anastasova, P. Vadgama, G.-Z. Yang, M.G. Boutelle, 3D printed microfluidic device with integrated biosensors for online analysis of subcutaneous human microdialysate, Anal. Chem. 87 (2015) 7763–7770.

[8] L.E. Murr, S. Gaytan, F. Medina, H. Lopez, E. Martinez, B. Machado, D. Hernandez, L. Martinez, M. Lopez, R. Wicker, Next-generation biomedical implants using additive manufacturing of complex, cellular and functional mesh arrays, Phil. Trans. R. Soc. A 368 (2010) 1999–2032.

[9] T. Laumer, K. Wudy, M. Drexler, P. Amend, S. Roth, D. Drummer, M. Schmidt, Fundamental investigation of laser beam melting of polymers for additive manufacture, J. Laser Appl. 26 (2014) 042003.

[10] G. Strano, L. Hao, R.M. Everson, K.E. Evans, Surface roughness analysis, modelling and prediction in selective laser melting, J. Mater. Process. Technol. 213 (2013) 589–597.

[11] F. Verhaeghe, T. Craeghs, J. Heulens, L. Pandelaers, A pragmatic model for selective laser melting with evaporation, Acta Mater. 57 (2009) 6006–6012.

[12] S.A. Khairallah, A.T. Anderson, A. Rubenchik, W.E. King, Laser powder-bed fusion additive manufacturing: Physics of complex melt flow and formation mechanisms of pores, spatter, and denudation zones, Acta Mater. 108 (2016) 36–45.

[13] L.L. Parimi, G. Ravi, D. Clark, M.M. Attallah, Microstructural and texture development in direct laser fabricated IN718, Mater. Charact. 89 (2014) 102–111.

[14] J. Smith, W. Xiong, W. Yan, S. Lin, P. Cheng, O.L. Kafka, G.J. Wagner, J. Cao, W.K. Liu, Linking process, structure, property, and performance for metal-based additive manufacturing: computational approaches with experimental support, Comput. Mech. 57 (2016) 583–610.

[15] Y. Lian, S. Lin, W. Yan, W.K. Liu, G.J. Wagner, A parallelized three-dimensional cellular automaton model for grain growth during additive manufacturing, Comput. Mech. 61 (2018) 543–558.

[16] Y. Zhang, G. Guillemot, M. Bernacki, M. Bellet, Macroscopic thermal finite element modeling of additive metal manufacturing by selective laser melting process, Comput. Methods Appl. Mech. Engrg. 331 (2018) 514–535.

[17] M. Russell, A. Souto-Iglesias, T. Zohdi, Numerical simulation of laser fusion additive manufacturing processes using the SPH method, Comput. Methods Appl. Mech. Engrg. 341 (2018) 163–187.

[18] N.T. Aboulkhair, N.M. Everitt, I. Ashcroft, C. Tuck, Reducing porosity in alsi10mg parts processed by selective laser melting, Addit. Manuf. 1 (2014) 77–86.

[19] M. Ma, Z. Wang, M. Gao, X. Zeng, Layer thickness dependence of performance in high-power selective laser melting of 1Cr18Ni9Ti stainless steel, J. Mater Process. Technol. 215 (2015) 142–150.

[20] L. Thijs, K. Kempen, J.-P. Kruth, J. Van Humbeeck, Fine-structured aluminium products with controllable texture by selective laser melting of pre-alloyed AlSi10Mg powder, Acta Mater. 61 (2013) 1809–1819.

[21] H. Exner, M. Horn, A. Streek, F. Ullmann, L. Hartwig, P. Regenfuß, R. Ebert, Laser micro sintering: A new method to generate metal and ceramic parts of high resolution with sub-micrometer powder, Virtual Phys. Prototyping 3 (2008) 3–11.

[22] T. Childs, C. Hauser, M. Badrossamay, Selective laser sintering (melting) of stainless and tool steel powders: experiments and modelling, Proc. Inst. Mech. Eng. B 219 (2005) 339–357.

[23] H. Schleifenbaum, W. Meiners, K. Wissenbach, C. Hinke, Individualized production by means of high power selective laser melting, CIRP J. Manuf. Sci. Technol. 2 (2010) 161–169.

[24] E. Yasa, J.-P. Kruth, J. Deckers, Manufacturing by combining selective laser melting and selective laser erosion/laser re-melting, CIRP Ann. 60 (2011) 263–266.

[25] H. Mindt, O. Desmaison, M. Megahed, Modelling Powder Bed Additive Manufacturing Defects, in: Proc 7th European Conference for Aeronautics and Space Sciences, 2017, 1-6.

[26] R. Ganeriwala, T.I. Zohdi, A coupled discrete element-finite difference model of selective laser sintering, Granul. Matter 18 (2016) 21.

[27] D. Bourell, B. Stucker, A. Spierings, N. Herres, G. Levy, Influence of the particle size distribution on surface quality and mechanical properties in AM steel parts, Rapid Prototyping J. (2011).

[28] J. Metelkova, Y. Kinds, K. Kempen, C. de Formanoir, A. Witvrouw, B. Van Hooreweder, On the influence of laser defocusing in selective laser melting of 316l, Addit. Manuf. 23 (2018) 161–169.

[29] C. Qiu, C. Panwisawas, M. Ward, H.C. Basoalto, J.W. Brooks, M.M. Attallah, On the role of melt flow into the surface structure and porosity development during selective laser melting, Acta Mater. 96 (2015) 72–79.

[30] R. Li, J. Liu, Y. Shi, L. Wang, W. Jiang, Balling behavior of stainless steel and nickel powder during selective laser melting process, Int. J. Adv. Manuf. Technol. 59 (2012) 1025–1035.

[31] H. Ali, L. Ma, H. Ghadbeigi, K. Mumtaz, In-situ residual stress reduction, martensitic decomposition and mechanical properties enhancement through high temperature powder bed pre-heating of selective laser melted ti6al4v, Mater. Sci. Eng. A 695 (2017) 211–220.

[32] Y. Li, D. Gu, Parametric analysis of thermal behavior during selective laser melting additive manufacturing of aluminum alloy powder, Mater. Des. 63 (2014) 856–867.

[33] H.Y. Jung, S.J. Choi, K.G. Prashanth, M. Stoica, S. Scudino, S. Yi, U. Kühn, D.H. Kim, K.B. Kim, J. Eckert, Fabrication of Fe-based bulk metallic glass by selective laser melting: A parameter study, Mater. Des. 86 (2015) 703–708.

[34] A. Okunkova, M. Volosova, P. Peretyagin, Y. Vladimirov, I. Zhirnov, A.V. Gusarov, Experimental approbation of selective laser melting of powders by the use of non-Gaussian power density distributions, Physics Procedia 56 (2014) 48–57.

[35] I. Yadroitsev, L. Thivillon, P. Bertrand, I. Smurov, Strategy of manufacturing components with designed internal structure by selective laser melting of metallic powder, Appl. Surf. Sci. 254 (2007) 980–983.

[36] H. Shipley, D. McDonnell, M. Culleton, R. Coull, R. Lupoi, G. O'Donnell, D. Trimble, Optimisation of process parameters to address fundamental challenges during selective laser melting of Ti-6Al-4V: A review, Int. J. Mach. Tools Manuf. 128 (2018) 1–20.

[37] C. Qiu, N.J. Adkins, M.M. Attallah, Microstructure and tensile properties of selectively laser-melted and of HIPed laser-melted Ti–6Al–4V, Mater. Sci. Eng. A 578 (2013) 230–239.

[38] M.F. Zaeh, G. Branner, Investigations on residual stresses and deformations in selective laser melting, Prod. Eng. 4 (2010) 35–45.

[39] Q. Chen, J. Liu, X. Liang, A.C. To, A level-set based continuous scanning path optimization method for reducing residual stress and deformation in metal additive manufacturing, Comput. Methods Appl. Mech. Engrg. 360 (2020) 112719.

[40] Z. Wang, M. Liu, Dimensionless analysis on selective laser melting to predict porosity and track morphology, J. Mater Process. Technol. 273 (2019) 116238.

[41] M. Rombouts, J.-P. Kruth, L. Froyen, P. Mercelis, Fundamentals of selective laser melting of alloyed steel powders, CIRP Ann. 55 (2006) 187–192.

[42] P.S. Cook, A.B. Murphy, Simulation of melt pool behaviour during additive manufacturing: Underlying physics and progress, Addit. Manuf. 31 (2020) 100909.

[43] Y.-C. Wu, W.-S. Hwang, C.-H. San, C.-H. Chang, H.-J. Lin, Parametric study of surface morphology for selective laser melting on Ti6Al4V powder bed with numerical and experimental methods, Int. J. Mater. Form. 11 (2018) 807–813.

[44] A.M. Rausch, V.E. Küng, C. Pobel, M. Markl, C. Körner, Predictive simulation of process windows for powder bed fusion additive manufacturing: Influence of the powder bulk density, Materials 10 (2017) 1117.

[45] A.J. Pinkerton, An analytical model of beam attenuation and powder heating during coaxial laser direct metal deposition, J. Phys. D: Appl. Phys. 40 (2007) 7323.

[46] B. Schoinochoritis, D. Chantzis, K. Salonitis, Simulation of metallic powder bed additive manufacturing processes with the finite element method: A critical review, Proc. Inst. Mech. Eng. B 231 (2017) 96–117.

[47] W.E. King, A.T. Anderson, R.M. Ferencz, N.E. Hodge, C. Kamath, S.A. Khairallah, A.M. Rubenchik, Laser powder bed fusion additive manufacturing of metals; physics, computational, and materials challenges, Appl. Phys. Rev. 2 (2015) 041304.

[48] F. Gürtler, M. Karg, M. Dobler, S. Kohl, I. Tzivilsky, M. Schmidt, Influence of powder distribution on process stability in laser beam melting: Analysis of melt pool dynamics by numerical simulations, in: Int. Solid Free Form Fabr. Symp. Austin, TX, 2014, pp. 1099-1117.

[49] E. Attar, Simulation of selective electron beam melting processes, 2011.

[50] A. Klassen, A. Bauereiß, C. Körner, Modelling of electron beam absorption in complex geometries, J. Phys. D: Appl. Phys. 47 (2014) 065307.

[51] J.L. Tan, C. Tang, C.H. Wong, A computational study on porosity evolution in parts produced by selective laser melting, Metall. Mater. Trans. A 49 (2018) 3663–3673.

[52] Z. Wang, W. Yan, W.K. Liu, M. Liu, Powder-scale multi-physics modeling of multi-layer multi-track selective laser melting with sharp interface capturing method, Comput. Mech. 63 (2018) 649–661.

[53] X. Shi, J. Zhao, Practical estimation of compression behavior of clayey/silty sands using equivalent void-ratio concept, J. Geotechn. Geoenviron. Eng. 146 (2020) 04020046.

[54] A. Hager, M. Kanitz, J. Grabe, C. Kloss, C. Goniva, Unresolved CFD-dem in environmental engineering: submarine slope stability and other applications, 2017.

[55] T.I. Zohdi, Rapid simulation of laser processing of discrete particulate materials, Arch. Comput. Methods Eng. 20 (2013) 309–325.

[56] T.I. Zohdi, Additive particle deposition and selective laser processing-a computational manufacturing framework, Comput. Mech. 54 (2014) 171–191.

[57] T. Zohdi, On the thermal response of a laser-irradiated powder particle in additive manufacturing, CIRP J. Manuf. Sci. Technol. 10 (2015) 7783.

[58] T. Zohdi, Modeling and simulation of laser processing of particulate-functionalized materials, Arch. Comput. Methods Eng. 24 (2017) 89–113.

[59] T. Zohdi, Construction of a rapid simulation design tool for thermal responses to laser-induced feature patterns, Comput. Mech. 62 (2018) 393–409.

[60] T. Zohdi, Ultra-fast laser-patterning computation for advanced manufacturing of powdered materials exploiting knowledge-based heat-kernels, Comput. Methods Appl. Mech. Engrg. 343 (2019) 234–248.

[61] T. Zohdi, N. Castrillon, Variability of targeted material thermal responses to laser-induced heating in additive manufacturing, J. Manuf. Sci. Eng. 141 (2019).

[62] H. Wessels, T. Bode, C. Weißenfels, P. Wriggers, T. Zohdi, Investigation of heat source modeling for selective laser melting, Comput. Mech. 63 (2019) 949–970.

[63] J.-H. Cho, D.F. Farson, J.O. Milewski, K.J. Hollis, Weld pool flows during initial stages of keyhole formation in laser welding, J. Phys. D: Appl. Phys. 42 (2009) 175502.

[64] Y. Lee, W. Zhang, Modeling of heat transfer, fluid flow and solidification microstructure of nickel-base superalloy fabricated by laser powder bed fusion, Addit. Manuf. 12 (2016) 178–188.

[65] Y. Lee, Simulation of Laser Additive Manufacturing and Its Applications, The Ohio State University, 2015.

[66] Y. Lee, W. Zhang, Mesoscopic simulation of heat transfer and fluid flow in laser powder bed additive manufacturing, International Solid Free Form Fabrication Symposium, Austin, 2015, pp. 1154-1165.

[67] Y. Lee, M. Nordin, S. Babu, D. Farson, Influence of fluid convection on weld pool formation in laser cladding, Weld. J. 93 (2014) 292S.

[68] Y. Lee, D.F. Farson, Simulation of transport phenomena and melt pool shape for multiple layer additive manufacturing, J. Laser Appl. 28 (2016) 012006.

[69] A. Otto, H. Koch, R.G. Vazquez, Multiphysical simulation of laser material processing, Physics Procedia 39 (2012) 843–852.

[70] F.J. Gürtler, M. Karg, M. Dobler, S. Kohl, I. Tzivilsky, M. Schmidt, Influence of powder distribution on process stability in laser beam melting: Analysis of melt pool dynamics by numerical simulations, in: 25th Annual International Solid Freeform Fabrication Symposium & #65533; an Additive Manufacturing Conference, SFF 2014, 2014, pp. 1099–1117.

[71] F.J. Gürtler, M. Karg, K.H. Leitz, M. Schmidt, Simulation of laser beam melting of steel powders using the three-dimensional volume of fluid method, Physics Procedia 41 (2013) 881–886.

[72] A. Otto, H. Koch, K.-H. Leitz, M. Schmidt, Numerical simulations - a versatile approach for better understanding dynamics in laser material processing, Physics Procedia 12 (2011) 11–20.

[73] A. Otto, M. Schmidt, Towards a universal numerical simulation model for laser material processing, Physics Procedia 5 (2010) 35–46.

[74] M. Markl, C. Körner, Multiscale modeling of powder bed–based additive manufacturing, Annu. Rev. Mater. Res. 46 (2016) 93–123.

[75] C. Körner, E. Attar, P. Heinl, Mesoscopic simulation of selective beam melting processes, J. Mater Process. Technol. 211 (2011) 978–987.

[76] E. Attar, Simulation of selective electron beam melting processes simulation der selektiven elektronenstrahlschmelzprozesse, 2011.

[77] A. Klassen, T. Scharowsky, C. Körner, Evaporation model for beam based additive manufacturing using free surface lattice Boltzmann methods, J. Phys. D: Appl. Phys. 47 (2014).

[78] A. Klassen, V.E. Forster, C. Körner, A multi-component evaporation model for beam melting processes, Modelling Simulation Mater. Sci. Eng. 25 (2017).

[79] A. Klassen, A. Bauereiß, C. Körner, Modelling of electron beam absorption in complex geometries, J. Phys. D: Appl. Phys. 47 (2014).

[80] R. Ammer, M. Markl, U. Ljungblad, C. Körner, U. Rüde, Simulating fast electron beam melting with a parallel thermal free surface lattice Boltzmann method, Comput. Math. Appl. 67 (2014) 318–330.

[81] A. Klassen, V.E. Forster, V. Juechter, C. Körner, Numerical simulation of multi-component evaporation during selective electron beam melting of TiAl, J. Mater Process. Technol. 247 (2017) 280–288.

[82] C. Körner, A. Bauereiß, E. Attar, Fundamental consolidation mechanisms during selective beam melting of powders, Modelling Simulation Mater. Sci. Eng. 21 (2013).

[83] R. Ammer, U. Rüde, M. Markl, V. Jüchter, C. Körner, Validation experiments for LBM simulations of electron beam melting, Internat. J. Modern Phys. C 25 (2014).

[84] A.M. Rausch, V.E. Küng, C. Pobel, M. Markl, C. Körner, Predictive simulation of process windows for powder bed fusion additive manufacturing: Influence of the powder bulk density, Materials 10 (2017).

[85] E. Attar, C. Körner, Lattice Boltzmann model for thermal free surface flows with liquid–solid phase transition, Int. J. Heat Fluid Flow 32 (2011) 156–163.

[86] D. Riedlbauer, T. Scharowsky, R.F. Singer, P. Steinmann, C. Körner, J. Mergheim, Macroscopic simulation and experimental measurement of melt pool characteristics in selective electron beam melting of Ti-6Al-4V, Int. J. Adv. Manuf. Technol. 88 (2017) 1309–1317.

[87] A. Rai, H. Helmer, C. Körner, Simulation of grain structure evolution during powder bed based additive manufacturing, Addit. Manuf. 13 (2017) 124–134.

[88] A. Rai, M. Markl, C. Körner, A coupled cellular automaton–lattice Boltzmann model for grain structure simulation during additive manufacturing, Comput. Mater. Sci. 124 (2016) 37–48.

[89] M. Megahed, H.-W. Mindt, N. N'Dri, H. Duan, O. Desmaison, Metal additive-manufacturing process and residual stress modeling, Integr. Mater. Manuf. Innov. 5 (2016) 61–93.

[90] J.R. Ibarra Medina, Development and Application of a CFD Model of Laser Metal Deposition, University of Manchester, 2013.

[91] H. Mindt, O. Desmaison, M. Megahed, Modelling powder bed additive manufacturing defects, 2015.

[92] H.-W. Mindt, O. Desmaison, M. Megahed, A. Peralta, J. Neumann, Modeling of powder bed manufacturing defects, J. Mater. Eng. Perform. 27 (2018) 32–43.

[93] H. Mindt, M. Megahed, N. Lavery, M. Holmes, S. Brown, Powder bed layer characteristics: the overseen first-order process input, Metall. Mater. Trans. A 47 (2016) 3811–3822.

[94] N. N'Dri, H.-W. Mindt, B. Shula, M. Megahed, A. Peralta, P. Kantzos, J. Neumann, DMLS Process modelling and validation, in: TMS 2015 144th Annual Meeting & Exhibition, Springer, 2015, pp. 389–396.

[95] A. Peralta, M. Enright, M. Megahed, J. Gong, M. Roybal, J. Craig, Towards rapid qualification of powder-bed laser additively manufactured parts, Integr. Mater. Manuf. Innov. 5 (2016) 154–176.

[96] J. Zielinski, S. Vervoort, H.-W. Mindt, M. Megahed, Influence of powder bed characteristics on material quality in additive manufacturing, BHM Berg. Hüttenmänn. Mon. 162 (2017) 192–198.

[97] J. Zielinski, H.-W. Mindt, J. Düchting, J.H. Schleifenbaum, M. Megahed, Numerical and experimental study of Ti6Al4V components manufactured using powder bed fusion additive manufacturing, JOM 69 (2017) 2711–2718.

[98] M.J. Matthews, G. Guss, S.A. Khairallah, A.M. Rubenchik, P.J. Depond, W.E. King, Denudation of metal powder layers in laser powder bed fusion processes, Acta Mater. 114 (2016) 33–42.

[99] W. King, A.T. Anderson, R.M. Ferencz, N.E. Hodge, C. Kamath, S.A. Khairallah, Overview of modelling and simulation of metal powder bed fusion process at lawrence livermore national laboratory, Mater. Sci. Technol. 31 (2015) 957–968.

[100] C.D. Boley, S.A. Khairallah, A.M. Rubenchik, Calculation of laser absorption by metal powders in additive manufacturing, Appl. Opt. 54 (2015) 2477–2482.

[101] S.A. Khairallah, A. Anderson, Mesoscopic simulation model of selective laser melting of stainless steel powder, J. Mater Process. Technol. 214 (2014) 2627–2636.

[102] S. Ly, A.M. Rubenchik, S.A. Khairallah, G. Guss, M.J. Matthews, Metal vapor micro-jet controls material redistribution in laser powder bed fusion additive manufacturing, Sci. Rep. 7 (2017) 4085.

[103] P.J. DePond, G. Guss, S. Ly, N.P. Calta, D. Deane, S. Khairallah, M.J. Matthews, In situ measurements of layer roughness during laser powder bed fusion additive manufacturing using low coherence scanning interferometry, Mater. Des. 154 (2018) 347–359.

[104] A.A. Martin, N.P. Calta, J.A. Hammons, S.A. Khairallah, M.H. Nielsen, R.M. Shuttlesworth, N. Sinclair, M.J. Matthews, J.R. Jeffries, T.M. Willey, J.R.I. Lee, Ultrafast dynamics of laser-metal interactions in additive manufacturing alloys captured by in situ X-ray imaging, Mater. Today Adv. 1 (2019) 100002.

[105] A.A. Martin, N.P. Calta, S.A. Khairallah, J. Wang, P.J. Depond, A.Y. Fong, V. Thampy, G.M. Guss, A.M. Kiss, K.H. Stone, C.J. Tassone, J. Nelson Weker, M.F. Toney, T. van Buuren, M.J. Matthews, Dynamics of pore formation during laser powder bed fusion additive manufacturing, Nature Commun. 10 (2019) 1987.

[106] J. Ye, S.A. Khairallah, A.M. Rubenchik, M.F. Crumb, G. Guss, J. Belak, M.J. Matthews, Energy coupling mechanisms and scaling behavior associated with laser powder bed fusion additive manufacturing, Adv. Energy Mater. 21 (2019).

[107] P. Bidare, I. Bitharas, R. Ward, M. Attallah, A.J. Moore, Fluid and particle dynamics in laser powder bed fusion, Acta Mater. 142 (2018) 107–120.

[108] C. Panwisawas, C. Qiu, M.J. Anderson, Y. Sovani, R.P. Turner, M.M. Attallah, J.W. Brooks, H.C. Basoalto, Mesoscale modelling of selective laser melting: Thermal fluid dynamics and microstructural evolution, Comput. Mater. Sci. 126 (2017) 479–490.

[109] C. Panwisawas, B. Perumal, R.M. Ward, N. Turner, R.P. Turner, J.W. Brooks, H.C. Basoalto, Keyhole formation and thermal fluid flow-induced porosity during laser fusion welding in titanium alloys: Experimental and modelling, Acta Mater. 126 (2017) 251–263.

[110] C. Panwisawas, Y. Sovani, R.P. Turner, J.W. Brooks, H.C. Basoalto, I. Choquet, Modelling of thermal fluid dynamics for fusion welding, J. Mater Process. Technol. 252 (2018) 176–182.

[111] J. Tan, C. Tang, C. Wong, Study and modeling of melt pool evolution in selective laser melting process of SS316L, MRS Commun. 8 (2018) 1178–1183.

[112] A.A. Shirgaonkar, M.A. MacIver, N.A. Patankar, A new mathematical formulation and fast algorithm for fully resolved simulation of self-propulsion, J. Comput. Phys. 228 (2009) 2366–2390.

[113] V.R. Voller, C. Prakash, A fixed grid numerical modelling methodology for convection–diffusion mushy region phase-change problems, Int. J. Heat Mass Transfer 30 (1987) 1709–1719.

[114] Z. Wang, K. Walayat, M. Liu, A velocity corrected unresolved CFD-DEM coupled method to reproduce wake effects at moderate Reynolds number, Eng. Comput. (2019).

[115] A. Di Renzo, F.P. Di Maio, Comparison of contact-force models for the simulation of collisions in DEM-based granular flow codes, Chem. Eng. Sci. 59 (2004) 525–541.

[116] A.B. Stevens, C. Hrenya, Comparison of soft-sphere models to measurements of collision properties during normal impacts, Powder Technol. 154 (2005) 99–109.

[117] H. Zhu, Z. Zhou, R. Yang, A. Yu, Discrete particle simulation of particulate systems: theoretical developments, Chem. Eng. Sci. 62 (2007) 3378–3396.

[118] J. Zhao, T. Shan, Coupled CFD–DEM simulation of fluid–particle interaction in geomechanics, Powder Technol. 239 (2013) 248–258.

[119] A. Bérard, G.S. Patience, B. Blais, Experimental methods in chemical engineering: Unresolved CFD-dem, Can. J. Chem. Eng. 98 (2020) 424–440.

[120] S. Benyahia, M. Syamlal, T.J. O'Brien, Extension of hill–koch–ladd drag correlation over all ranges of Reynolds number and solids volume fraction, Powder Technol. 162 (2006) 166–174.

[121] K. Kafui, C. Thornton, M. Adams, Discrete particle-continuum fluid modelling of gas–solid fluidised beds, Chem. Eng. Sci. 57 (2002) 2395–2410.

[122] R.J. Hill, D.L. Koch, A.J. Ladd, The first effects of fluid inertia on flows in ordered and random arrays of spheres, J. Fluid Mech. 448 (2001) 213–241.

[123] A. Hager, C. Kloss, S. Pirker, C. Goniva, Parallel resolved open source CFD-DEM: method, validation and application, J. Comput. Multiph. Flows 6 (2014) 13–27.

[124] D. Fantin, CFD-DEM Coupling for Systems of Fluid and Non-Spherical Particles, Delft University of Technology, Delft, 2018.

[125] H. Wessels, C. Weißenfels, P. Wriggers, Metal particle fusion analysis for additive manufacturing using the stabilized optimal transportation meshfree method, Comput. Methods Appl. Mech. Engrg. 339 (2018) 91–114.

[126] J. Roenby, H. Bredmose, H. Jasak, A computational method for sharp interface advection, R. Soc. Open Sci. 3 (2016) 160405.

[127] M. Rudman, A volume-tracking method for incompressible multifluid flows with large density variations, Int. J. Numer. Methods Fluids 28 (1998) 357–378.

[128] M. Rudman, Volume-tracking methods for interfacial flow calculations, Internat. J. Numer. Methods Fluids 24 (1997) 671–691.

[129] Z.S. Saldi, Marangoni driven free surface flows in liquid weld pools, 2012.

[130] J.U. Brackbill, D.B. Kothe, C. Zemach, A continuum method for modeling surface tension, J. Comput. Phys. 100 (1992) 335–354.

[131] J.L. Tan, C. Tang, C.H. Wong, Study and modeling of melt pool evolution in selective laser melting process of SS316L, MRS Commun. 8 (2018) 1178–1183.

[132] V.R. Voller, M. Cross, N. Markatos, An enthalpy method for convection/diffusion phase change, Internat. J. Numer. Methods Engrg. 24 (1987) 271–284.

[133] F. Rösler, D. Brüggemann, Shell-and-tube type latent heat thermal energy storage: numerical analysis and comparison with experiments, Heat Mass Transf. 47 (2011) 1027.

[134] A. Beer, Bestimmung der absorption des rothen lichts in farbigen flussigkeiten, Ann. Physics 162 (1852) 78–88.

[135] R. McVey, R. Melnychuk, J. Todd, R. Martukanitz, Absorption of laser irradiation in a porous powder layer, J. Laser Appl. 19 (2007) 214–224.

[136] T. Mukherjee, J. Zuback, A. De, T. DebRoy, Heat and fluid flow modeling to examine 3D-printability of alloys, in: 7th International Symposium on High-Temperature Metallurgical Processing, Springer, 2016, pp. 471–478.

[137] J.F. Ready, D.F. Farson, T. Feeley, LIA Handbook of Laser Materials Processing, 2001.

[138] G. Chris, 7.1 Thermophysical Models, OpenFOAM V5 User Guide, OpenFOAM Foundation, London, 2017.

[139] C. Goniva, C. Kloss, N.G. Deen, J.A. Kuipers, S. Pirker, Influence of rolling friction on single spout fluidized bed simulation, Particuology 10 (2012) 582–591.

[140] C. Kloss, C. Goniva, A. Hager, S. Amberger, S. Pirker, Models, Algorithms and validation for opensource DEM and CFD–DEM, Prog. Comput. Fluid Dyn. Int. J. 12 (2012) 140–152.

[141] R.I. Issa, Solution of the implicitly discretised fluid flow equations by operator-splitting, J. Comput. Phys. 62 (1986) 40–65.

[142] V. Vuorinen, J.-P. Keskinen, C. Duwig, B. Boersma, On the implementation of low-dissipative runge–kutta projection methods for time dependent flows using OpenFOAM®, Comput. & Fluids 93 (2014) 153–163.

[143] B. Blais, M. Lassaigne, C. Goniva, L. Fradette, F. Bertrand, A semi-implicit immersed boundary method and its application to viscous mixing, Comput. Chem. Eng. 85 (2016) 136–146.

[144] A. Hager, Cfd-Dem on Multiple Scales-an Extensive Investigation of Particle-Fluid Interactions, Johannes Kepler University Linz, Linz, 2014.

[145] Z. Zhou, S. Kuang, K. Chu, A. Yu, Discrete particle simulation of particle–fluid flow: model formulations and their applicability, J. Fluid Mech. 661 (2010) 482–510.

[146] J.J. Valencia, P.N. Quested, Thermophysical properties, in: ASM Handbook, ASM International, 2008.

[147] M. Reiner, The deborah number, Phys. Today 17 (1964) 62.

[148] R. Nandan, T. Lienert, T. DebRoy, Toward reliable calculations of heat and plastic flow during friction stir welding of Ti-6Al-4V alloy, Int. J. Mater. Res. 99 (2008) 434–444.

[149] L.F.L. Silva, P.L. Lage, Development and implementation of a polydispersed multiphase flow model in OpenFOAM, Comput. Chem. Eng. 35 (2011) 2653–2666.

[150] E. Frederix, M. Stanic, A.K. Kuczaj, M. Nordlund, B.J. Geurts, Extension of the compressible PISO algorithm to single-species aerosol formation and transport, Int. J. Multiph. Flow. 74 (2015) 184–194.

[151] J. Trapp, A.M. Rubenchik, G. Guss, M.J. Matthews, In situ absorptivity measurements of metallic powders during laser powder-bed fusion additive manufacturing, Appl. Mater. Today 9 (2017) 341–349.

[152] A.F. Kaplan, Local absorptivity modulation of a 1μm-laser beam through surface waviness, Appl. Surf. Sci. 258 (2012) 9732–9736.

[153] R. Li, J. Liu, Y. Shi, L. Wang, W. Jiang, Balling behavior of stainless steel and nickel powder during selective laser melting process, Int. J. Adv. Manuf. Technol. 59 (2011) 1025–1035.

[154] J. Stef, A. Poulon-Quintin, A. Redjaimia, J. Ghanbaja, O. Ferry, M. De Sousa, M. Gouné, Mechanism of porosity formation and influence on mechanical properties in selective laser melting of Ti-6Al-4V parts, Mater. Des. 156 (2018) 480–493.

[155] L. Thijs, F. Verhaeghe, T. Craeghs, J.V. Humbeeck, J.-P. Kruth, A study of the microstructural evolution during selective laser melting of Ti–6Al–4V, Acta Mater. 58 (2010) 3303–3312.

[156] J.-P. Kruth, X. Wang, T. Laoui, L. Froyen, Lasers and materials in selective laser sintering, Assem. Autom. (2003).

[157] S. Zhang, Q. Wei, L. Cheng, S. Li, Y. Shi, Effects of scan line spacing on pore characteristics and mechanical properties of porous Ti6Al4V implants fabricated by selective laser melting, Mater. Des. 63 (2014) 185–193.